A Comparison Study of the Transformation Behavior during Uniform Continuous Cooling and Hot Deformation Characteristics of a Wrought and Selective Laser Melting 4340 Steels

by

Yuankang Wang

BS, Materials Science and Engineering, Sichuan University, 2018

BS, Materials Science and Engineering, University of Pittsburgh, 2018

Submitted to the Graduate Faculty of the

Swanson School of Engineering in partial fulfillment

of the requirements for the degree of

Master of Science in Materials Science and Engineering

University of Pittsburgh

2020

UNIVERSITY OF PITTSBURGH

SWANSON SCHOOL OF ENGINEERING

This thesis was presented

by

Yuankang Wang

It was defended on

November 12, 2020

and approved by

Ian Nettleship, Ph.D., Associate Professor, Department of Mechanical Engineering and Materials Science

Susheng Tan, Ph.D., Associate Professor, Department of Electrical and Computer Engineering

Thesis Advisor: C. Issac Garcia, Ph.D., Professor, Department of Mechanical Engineering and Materials Science

A Comparison Study of the Transformation Behavior during Uniform Continuous Cooling and Hot Deformation Characteristics of a Wrought and Selective Laser Melting 4340 Steels

Yuankang Wang, MS

University of Pittsburgh, 2020

This study compares the Austenite Grain Growth Behavior and its Transformation Behavior during the uniform Continuous Cooling of a Selective Laser Melting (SLM) 4340 and conventional Wrought 4340 steels. SLM 4340 steels exhibit inferior mechanical properties then conventional Wrought 4340 steels. Hence, the effect of hot deformation on the final microstructure and mechanical properties of SLM 4340 steel were also investigated in this study. Standard dilatometry testing was used to study the Austenite decomposition behavior at different cooling rates and to develop the CCT diagrams. Hot Compression Testing was performed to investigate the effect of hot deformation on the microstructure of austenite for both systems SLM 4340 and Wrought 4340. Advanced microstructural characterization techniques, Scanning Electron Microscopy (SEM) and Orientation Imaging Microscopy (OIM) were employed to support the CCT diagrams. Electron Backscatter Diffraction (EBSD) and a special EBSD-IQ characterization technique were used to assess the percentage of the microstructural components observed. Three important observations were made: 1) the hardenability of the Wrought 4340 steel was higher than the SLM 4340 steel; 2) the presence of Granular Bainite was observed after slow cooling conditions in both steels. MTEXT, a MATLAB program, was used to reconstruct the prior Austenite grains (PAG). The SLM steel exhibited finer Austenite grain size distribution than the Wrought steel in the temperature range studied; and 3) the porosity in SLM 4340 was closed during the hot compression tests improving its mechanical properties. The level of microstructural

refinement of austenite after hot deformation was measured by the effective interfacial area per unit volume (Sv) parameter for the SLM 4340 and Wrought 4340 steels.

Table of Contents

List of Tables

List of Figures

Acknowledgement

Throughout thew whole project and writing of this thesis I have received a great deal of support and assistance from many people. It is impossible for me to accomplish this study without their support.

I would first like to express my deepest appreciation to my advisor, Professor C. Issac Garcia, whose expertise in physical metallurgy is priceless and always the most important support for me to finish this study. Your insightful comment and guidance in every technical meeting push me to sharpen my thinking and improve myself.

I would like to thank my partner Pedro de Souza Ciacco and my mentor Dr. Zhou. Pedro helped me a lot in sample preparation, microstructure analysis, and our co-work brought this project to a higher level. Dr. Zhou provided me with lots of literatures which guided me to find the right direction and completed this thesis successfully.

I would also like to thank Dr. Raymundo and ELLWOOD Group for providing experimental materials and helping us to finish some experiments which cannot be done in lab. Special thanks to FIERF for funding this project.

I'd like to acknowledge the assistance of Luis Fellipe Simoes and Dr. Solis Bravo for their guidance throughout the studies. You provided me with basic skills I needed to learn in this lab. Thanks also to University of Pittsburgh for providing training and necessary facilities.

In addition, I would like to thank my parents. Without their education and support, I would not have chance to came to University of Pittsburgh and work with these talented people.

1.0 Introduction

4340 steel is a low alloy steel containing chromium, nickel and molybdenum. Because of its high strength and toughness, this steel is commonly used in the forging industry for the manufacture of structural components for the defense, aerospace, energy and automotive industries [1-8]. The great majority of the components are made from Wrought 4340 steel. This conventional processing technology is well-understood, accepted and applied around the world. Selective laser melting is a kind of additive manufacturing technology, which is widely used in industry because of its no restriction on design and versatility on manufacturing. This approach allows one to manufacture components from CAD file and build up the components layer by layer. Use of AM technology could solve some of the problems observe in Wrought 4340 steel like non-uniform chemical composition, better cleanliness of non-metallic inclusions, i.e. (MnS).

This Project involved 4340 Steels fabricated using two distinct processing routes, one is the conventional wrought 4340 steel and the other 4340 steel was manufactured by selective laser melting technology. The particular processing parameters will be described in more detail in the following sections.

2.0 Problem Statement

In the United States, AM technology has already been incorporated in manufacturing. For example, in aerospace industry, AM can help the aerospace industry to optimize parts, lower the weight, and reduce material loss [15]. In the medical field, the AM technology is widely used to produce metal-ceramic dental restorations and artificial organs [16]. However, high manufacturing cost and poor mechanical properties of additive manufactured steel components caused by porosity and discontinuities [17] has limited the application of AM technology in the steel industry. Therefore, problems like these have slowed down the development of AM technology in certain steels systems. The 4340 steel grade is one example, there is a dearth of information of manufacturing stage in the open literature, no paper reports austenite grain growth behavior and continuous cooling transformation behavior of additive manufactured 4340 steel which are important to industry. Also, few papers investigated the effect of porosity caused by AM on austenite grain growth and continuous cooling behavior in this steel type.

The aim of this thesis is to conduct a comprehensive study of SLM 4340 and Wrought 4340 comparing the austenite grain growth behavior and its transformation behavior during continuous cooling and gain an understanding of the resulting final microstructures. This information can be used for future studies.

3.0 Hypothesis

The presence of porosity which results from AM processing can have great influence in the low and high temperature behavior of the microstructure of SLM 4340 components. For example, the presence of can have significant pinning effect on the austenite grain growth during heat treatment.

Hypothesis 1. Porosity in SLM 4340 provides the pinning force to inhibit austenite grain growth during reheating conditions, hence finer prior austenite grain size is obtained. Also, finer prior austenite grain size results in lower hardenability, favoring the formation of high temperature transformation products under certain cooling rates. The CCT diagram for this alloy will be shifted to the left.

The pinning effect of porosity during austenitization treatments will result in finer microstructure austenite. However, the presence of pores might also act as strong stress-raisers and lead to poor strength and ductility. Hot deformation will be used in this project to eliminate porosities by closing them.

Hypothesis 2. After hot deformation, the SLM 4340 is expected to have finer microstructure than Wrought 4340 and porosity is eliminated by deformation. These factors might enhance the mechanical properties of SLM 4340 compared to wrought 4340.

4.0 Literature Review

4.1 AISI 4340 Steels

AISI 4340 is a medium carbon, low alloy steel known for its toughness and strength. Table 1 shows the typical chemical composition of AISI 4340 under US standard. Quenched and Tempered (Q&T) processing is the most common heat treatment for hardening and strengthening of 4340 steel. The tensile range of 4340 alloy steel after Quenched & Tempered is generally between 930-1080MPa. Austempering is another heat treatment method to strengthen 4340 steel by obtaining bainite martensite microstructures [10], 4340 steel in the austempered condition could exhibit higher tensile stress and toughness than Q&T 4340 steel [11]. They are well-known for their excellent shock, impact, wear and abrasion resistance in the as-heat treated condition. In addition, this grade of steel can exhibit good fatigue strength levels, combined with adequate atmospheric corrosion resistance. This grade of steel is widely used in structural parts.

Table 1 Chemical Composition of AISI 4340

C	Mn	P	S	Si	Ni	Cr	Mo
0.38-0.43	0.60-0.80	0.035	0.040	0.15-0.35	1.65-2.00	0.70-0.90	0.20-0.30

4.2 Additive Manufacturing

Additive manufacturing (AM) technology, has been labeled by different names, such as three-dimensional (3D) printing, rapid prototyping (RP), layered manufacturing (LM) and solid freedom fabrication [12], is an approach where 3D components can be built from 3D design software, i.e. CAD and SolidWorks without any specific tools. In this layer by layer fabrication, each layer is built along the X-Y directions with constant thickness in the Z direction. Since its inception AM technology showed to be a revolutionary technology, its expanding and continues to grow steadily. In 2012, the market was about $200 million dollars [13] and the global additive manufacturing market grew in 2019 to over $10.4 billion dollars [14].

In this study, Selective Laser Melting (SLM), a kind of Powder Deposition-Based Techniques, is involved. In the SLM process, the metal powder is delivered to the melt pool with a recoater and argon gas. The powder melts in the liquid metal pool by laser energy resource and argon could prevent oxidation and accelerate solidification. When the melt pool is solidified, the piston will move downward and print the next layer [18-24]. Figure 1 shows a schematic description of Selective Laser Melting Technology.

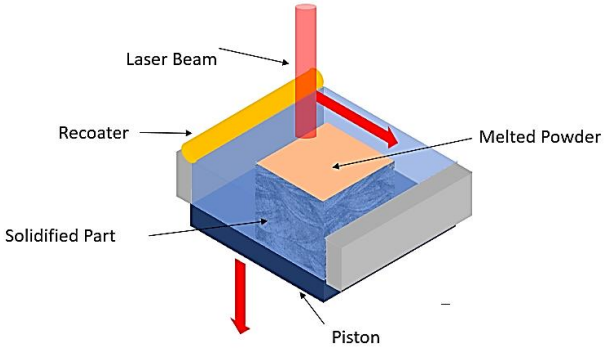

Figure 1 Selective Laser Melting Scheme

4.3 Austenite Grain Growth Behavior

Austenite grain growth takes place during the heat treatment process, prior to any hot deformation process, i.e. hot rolling or forging. The chemical composition of austenite and its microstructural condition (recrystallized or non-recrystallized) prior to transformation influences phase transformations, precipitation reactions and the mechanical properties, such tensile strength, impact toughness, hardness among other mechanical properties. Despite the importance of the austenite grain growth behavior in steel components, studies of austenite in additive manufactured steel components are scarce compared to investigations related to conventionally fabricated wrought 4340 steels. This thesis has observed substantial differences in the Austenite Grain Growth Behavior between SLM 4340 and Wrought 4340 steels. These differences provided guidance to subsequent work in this thesis.

4.4 Continuous Cooling Transformation Behavior of Recrystallized and Deformed Austenite

The performance of a steel depends on its chemical composition and microstructure. CCT diagram provides the relationship between cooling path and final microstructure. CCT diagram of SLM 4340 does not exist in the open literature. This work conducted in this thesis will be the first known study in this area. In this study, continuous cooling transformation behavior of SLM 4340 and Wrought 4340 are investigated in deformed and undeformed conditions. CCT diagrams were developed with the aid of standard dilatometry tests.

4.4.1 Pearlite Transformation

The austenite decomposition and transformation behavior under equilibrium conditions can be understood using the Fe-C diagram. This diagram provides the basic framework for understanding phase transformations and microstructures of steels. Figure 2 shows an example of the Fe-C diagram that contains decomposition of austenite using slow cooling rates. The microstructure of 4340 are completely austenite at all temperatures in the supercritical phase field region down to Ar3 temperature. If cooled very slowly through A3 temperature, the phase diagram shows part of austenite will transform to ferrite, and the carbon rejected during the ferrite formation will diffuse to enrich the untransformed austenite. When the temperature reaches A1 the untransformed austenite will be replaced by mixture of ferrite and cementite and produces a unique microstructure termed pearlite as shown in Figure 3.

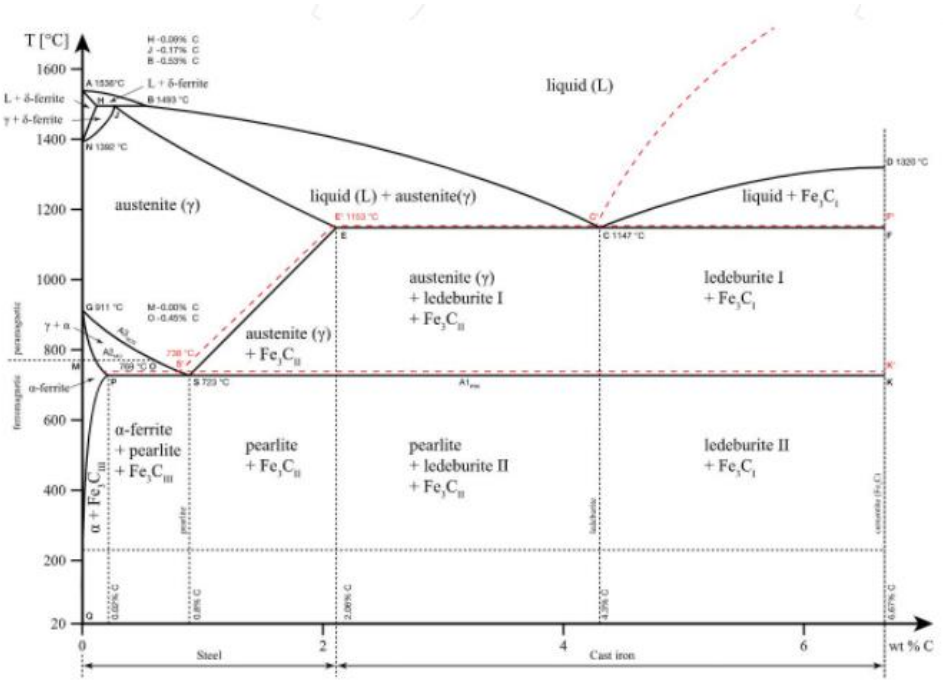

Figure 2 Fe-C Diagram

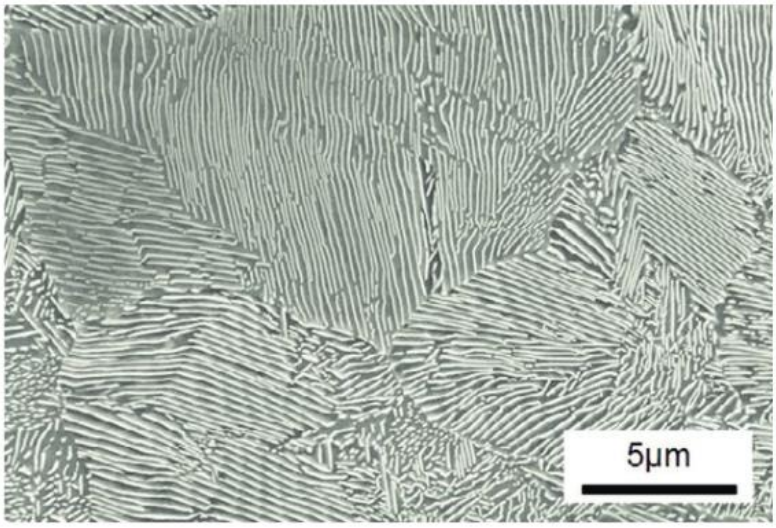

Figure 3 Microstructure of Pearlite Steel (SEM)

4.4.2 Martensite Transformation

Martensite is named after the German metallurgist, Adolf Marten, to designate hard microstructure found in quenched carbon steel [27]. The martensitic transformation is diffusionless, the atoms do not partition themselves during the transformation, therefore, the martensite have same chemical composition to their parent austenite. In martensitic transformation, the atom will not diffuse, but instead are trapped in the octahedral sites of a body-centered cubic structure [28]. The temperature that austenite starts to form martensite is called the martensite start temperature (Ms). The Ms reflects the amount of thermodynamic driving force to initiate the transformation of austenite to martensite, and it is highly influenced by carbon content [29]. Mf is the temperature at which the martensite transformation is completed. In this study, Ms and Mf temperature were measured by dilatometry tests.

4.4.3 Bainite Transformation

At the temperature between the transformation of austenite to pearlite and the transformation of austenite to martensite, bainite is formed. The start temperature of bainite transformation (Bs) could be determined by the equation of alloy content [30] or experimental method like dilatometry test.

There are two kinds of bainite form in different temperature range. Upper bainite form at the temperature just below the formation of pearlite, and lower bainite form at the lower temperature. Like pearlite, bainite is also a microstructure combined of ferrite and cementite. In upper bainite, carbon diffuse into austenite completely during transformation, however, this process cannot be completed at lower temperatures. Therefore, the carbon precipitate in ferrite can

be observed in lower bainite. Figure 4 is a schematic representation of the transition from upper to lower bainite.

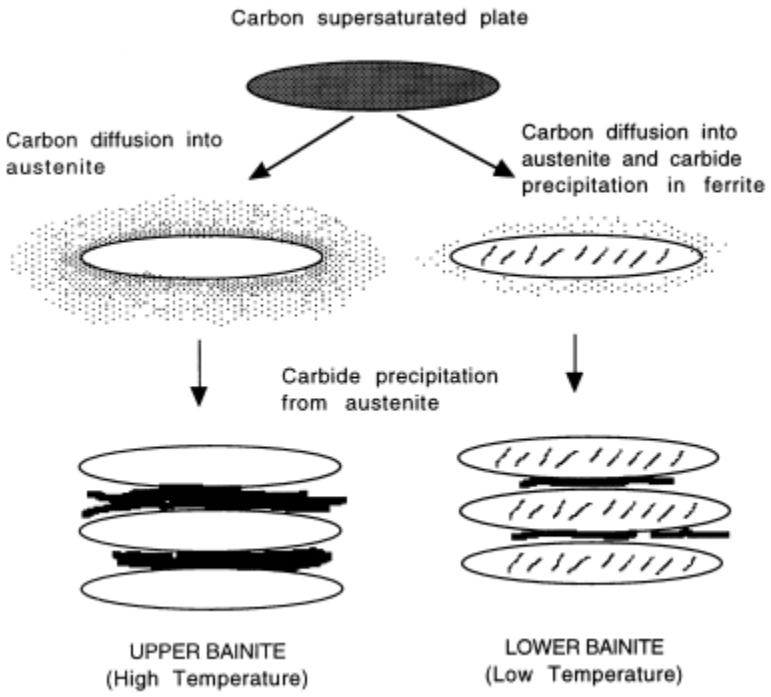

Figure 4 Schematic representation of Bainite Transformation

4.4.4 Dilatometry Test

Dilatometry is one of the powerful techniques to study phase transformation in steels to determine phase transformation temperatures on heating (Ac1, Ac3) and cooling (Fs, Ps, Pf, Bs, Bf, Ms, Mf) with differential thermal analysis and quantitative analysis of microstructures.

The phase transformation temperature can be determined easily by dilatometry test due to the specific volume change during the phase transformation. During the phase transformation, the lattice structure changes causes the specific volume change. In continuous heating process, the volume of steel increases with temperature linearly, when phase transformation happened, the

initial microstructure starts to transform to austenite, which is Face-centered microstructure. FCC has higher atomic packing factor than BCC, so the volume will shrink during the transformation of the initial microstructure. During continuous cooling process, the volume expansion corresponds to the transformation of austenite into ferrite, pearlite, bainite or martensite.

4.5 Hot Deformation

The main objective of hot deformation in modern steels is to control the chemical composition and microstructural condition of austenite prior to its transformation behavior. This process is essential to refine the final microstructure and to meet different performance requirements. In this study, hot deformation was used to eliminate the porosity in SLM 4340 to improve the mechanical properties. The increase of nucleation sites for the γ-α transformation depends on the amount of deformation in non-recrystallization region, expressed by effective interfacial area per unit volume (Sv) [32,33]. If hot deformation takes place under recrystallization temperature, the Sv is comprised of two terms: the area of elongated austenite grain boundaries per unit volume (Sv.gb) and the area of deformation bands and twins per unit volume inside austenite grains (Sv.IPD). Sv for hot deformation under recrystallization temperature is determined by the equation [34]:

$$Sv=[1.67(\varepsilon-0.10)+1]\,(2/d)+63(\varepsilon-0.30) \quad (4\text{-}1)$$

ε is the strain below recrystallization temperature, d is the equiaxed grain diameter prior to the uncrystallized hot deformation.

4.6 Chemical Etchants

Three different kinds of chemical etchants were used in this study for different purposes. Nital is a widely used etchant to reveal end microstructure of steels. The concentration of Nital is adjusted based on the corrosion resistance of steel. Solidum metabisulfite is used to color the martensite and bainite. Martensite and bainite are hard to distinguished under optical microscopy, however, solidum metabisulfite can be used to etch a wide range of steel compositions and creates a strong contrast between bainite (brown) and martensite (blue) under polarized light microscopy [35]. In determining prior austenite grain boundaries, picric acid is widely used to reveal prior austenite grain growth. Ryan Barrows [38] reported positive results etching quenched and tempered 4340 with a reagent of 100ml saturated aqueous picric acid, 0.4 mL of HCl, 1g of wetting agent.

4.7 Porosity Density Measurement: Archimedes Method

Archimedes method is a classic approach to determine the density of a sample. In this method, the sample is fully immersed into liquid, the buoyant force on the sample is equal to the weight of the displaced fluid. Because wrought 4340 does not contain porosity and have similar chemical composition with SLM 4340, assume the density of wrought 4340 and SLM 4340 (without porosity) are identical. Compare actual volume and ideal volume of 4340, the porosity could be measured:

$$V_{actual}=m_{in\ air}-m_{in\ water}/\rho_{water} \quad (4\text{-}2)$$

$$\text{porosity (volume fraction)} = (1-V_{ideal}/V_{actual}) \times 100\% \quad (4\text{-}3)$$

Where ρ_{water} is the density of water, ρ_{steel} is the density of wrought 4340, V_{actual} is actual volume of sample measured by Archimedes method, V_{ideal} is ideal volume if SLM 4340 is porosity free.

4.8 EBSD-IQ analysis

Image Quality (IQ) is an important parameter in the EBSD (Electron Backscatter Diffraction) technique. IQ is defined as the sum of the detected peaks in the Hough Transform, and describes the quality of an electron backscatter diffraction pattern. Different types of ferrite produced at different temperatures during cooling will have different densities of dislocations or sub-grain boundaries. For example, Martensite has very low IQ value. The index chosen to distinguish the degree of lattice imperfection is image quality (IQ), a lattice distorted by crystalline defects such as dislocations and sub-grain boundaries will have a distorted Kikuchi Pattern, leading to a lower IQ value. Both the types of ferrite and the IQ level of the individual ferrite grains vary with dislocation density, so the measurement of the spectrum of IQ values in a given samples is necessary.

Assume a normal distribution with a mean and standard deviation represents a single microconstituent. Dividing the whole distribution into several normal distributions, each of normal

distribution represents a certain microconstituent and the fraction of each normal distribution represents the fraction of each microconstituent in microstructure [37].

5.0 State of Objectives

The aim of this thesis is to conduct a comprehensive study comparing the austenite grain growth behavior and its transformation behavior during continuous cooling and gain an understanding of the resulting final microstructures of Wrought 4340 and SLM 4340.

At first, in order to get the basic understanding of Selective Laser Melting 4340 to design following experiment. The microstructure analysis, austenite grain growth behavior of SLM 4340 and Wrought 4340 are compared. Also, the porosity density of SLM 4340 is measured.

The second objective is to develop continuous cooling transformation behavior diagrams and compare final microstructure under each cooling rate of these steels. To achieve that, dilatometry technique is used to develop CCT diagram. Microstructure characterizations are conducted with optical microscopy, scanning electron microscopy, and KAM, EBSD-IQ analysis from electron back-scatter diffraction patterns.

The final part is to investigate the effect of hot deformation on both steels. Sv value are measured to quantify strain energy and nucleation site of deformed austenite. The microstructure of hot-deformed SLM and wrought 4340 under different cooling rate would be great help to understand the effect of different manufacturing technology on mechanical properties.

6.0 Experimental Method

Table 2 shows the chemical composition of the two steels being studied in this program. the compositions are very similar, except for the higher content in the Nitrogen and Oxygen content in the SLM 4340 steel compared to Wrought 4340 steel. The samples from the Wrought steel were produced from an initial ingot size of 101.6cm x 134.62cm. The ingot was reheated at 1176°C and reduced to 45.72cm x 45.72cm square round corner and air cooling to room temperature. Subsequently heat treated at 621°C for 2 hours then air cooling to room temperature. Sections from this ingot were cut and provided for our study. The size of the samples received are shown in Table 3. Figure 5 shows a schematic representation of the samples received.

Table 2 Chemical Composition of 4340 Steels

	C	Mn	P	S	Si	Ni	Cr	Mo
Wrought	0.42	0.75	0.013	0.008	0.31	1.75	0.85	0.27
	V	Cu	Al					
	0.006	0.22	0.021					
	C	Mn	P	S	Si	Ni	Cr	Mo
SLM	0.41	0.78	0.010	0.004	0.33	1.87	0.88	0.24
	N	O						
	0.02	0.07						

Table 3 Dimenstion of As-received Materials (cm)

	Length	Width	Height
Wrought 4340	23.5	23.5	5.0
SLM 4340	23.4	15.7	2.3

Figure 5 3D model of as-received 4340 (left is Wrought 4340, right is SLM 4340)

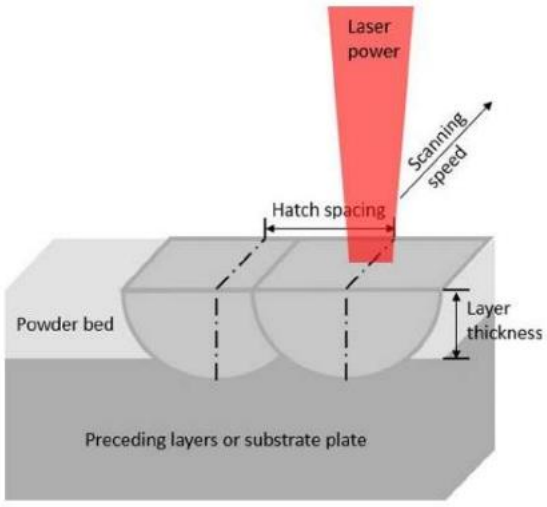

Figure 6 Important Process Parameters of SLM

6.1 Reheating Studies

Austenitization was done under Argon conditions to minimize oxidation. Samples from each steel starting condition were austenitized at 850°C, 950°C, 1050°C, and 1150°C for 1 hour, then water quenched. The resulting specimens were cut in half, so half was used for Prior-Austenitic Grain Size measurements. The PAGS was revealed by etching the specimens with a Picral solution containing 100 ml of distilled de-ionized water, picric acid to saturation, 2g of sodium dodecyl benzenesulfonate and 6 drops of hydrochloric acid. Etching was done in ultrasonic cleaner. Samples are soaked in etching reagent for 7 minutes. If prior austenite grain boundaries are not clear under optical microscopy, light polish the sample with water for 1minute then do another 7 minutes etching. Repeat this procedure until prior austenite grain boundaries are completely revealed.

6.2 Dilatometry Test

The samples used for dilatometric studies were machined from the as-received conditions into cylinders approximately 3mm in diameter and 10mm in length. A total of 17 samples were studied, eight (8) from SLM 4340 and nine (9) from Wrought 4340. Each sample were reheated to 900°C with a heating rate of 50 C/min and a soaking time of 15min prior to uniform cooling. Then samples were cooled using different cooling rates: (1) 0.25°C/min, (2) 0.5°C/min, (3) 1°C/min, (4) 5°C/min, (5) 10°C /min, (6) 20°C/min, (7) 50°C/min, (8) 100°C/min and (9) 200°C/min, as shown in Figure 7.

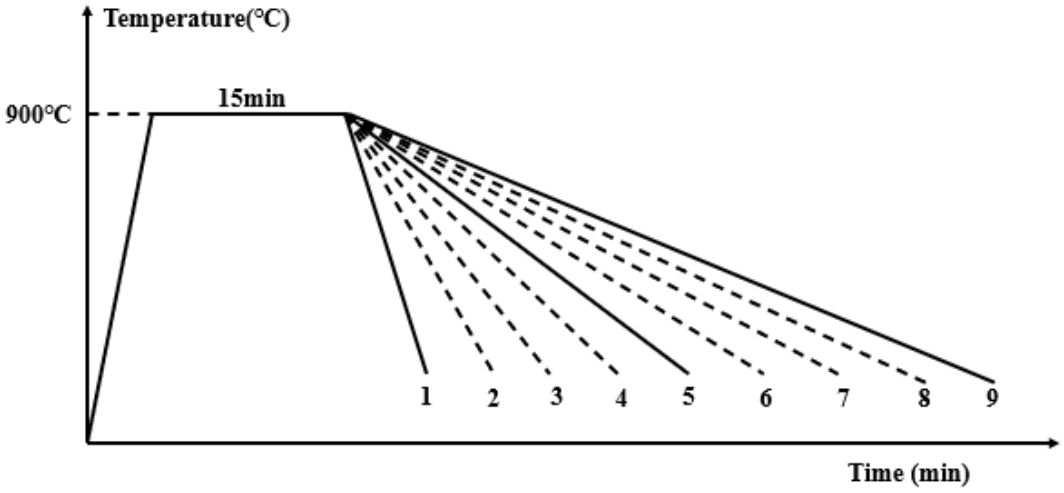

Figure 7 Scehematic Cycle for the Dilatometry Tests

All the dilatometry tests were done using a LINSEIS L78 Machine (Figure 8) coupled with an induction furnace. The temperature range of the system is between -150°C to 1600°C, with heating rates up to 4000K/s and cooling rates up to 4000K/s, approximately. After the dilatometry tests, the samples were subjected to microstructural analysis.

Figure 8 Equipment Used for Dilatometry Tests (LINESEIS L78 Machine)

6.3 Hot Deformation

Cylindrical samples were machined with a height-to-diameter ratio of 1.5. this ratio in several research was selected for the specimens to ensure homogeneous deformation [39]. Their dimensions are of 1.9cm height and 1.27cm diameter, as shown in Figure 9. The samples have a small diameter hole at the mid-height where a thermocouple is attached. In addition, the top and bottom of the sample a small reservoir was machined. This geometry will contain a special lubricant to reduce barreling during hot deformation testing. A total of 12 compression samples from steel wrought and SLM 4340 were machined.

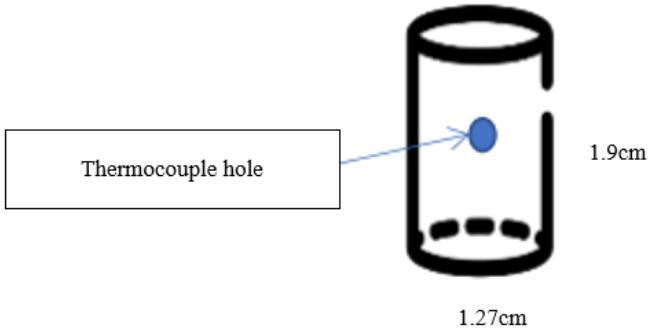

Figure 9 Schematic Representation of Compression Samples

6.3.1 Nickel Plating

Prior to hot compression testing the samples were protected against oxidation. This process includes the following steps: 1) removal of oxides, using a pickling solution, and 2) Nickel plating. The pickling solution contained 100mL of hydrochloric acid and 100mL of deionized water (Pickling - 50% HCl and 50% H2O). All samples were immersed for approximately 5 minutes.

The Nickel plating consisted of immersing the samples in Nickel solution containing 18.25mL of Electroless Nickel (Part A), 56.75mL of Electroless Nickel/Cobalt (Part B) and 300mL of deionized water (1 Part A + 3 Part B + 16.44 Part H2O – in volume). To activate the mixing process, the solution was heated on a hot plate to 90°C, also the temperature at which coating occurs. Once the desired temperature was reached, 6 samples were placed in a basket and immersed into the solution for 30 minutes. Figure 10 highlights this procedure with a comparison of samples before and after Nickel plating.

(a) (b) (c)

Figure 10 Nickel Plating (a)Nickel Plating procedure, (b)samples before Ni plating, (c)samples after Ni plating

6.3.2 Hot Compression Test

Hot compression tests were conducted under isothermal condition at three different cooling rates. All specimens are heated up to 1150℃ and held for 2mins and then cool to the 900℃, the deformation temperature. The samples were deformed to an engineering strain of 0.5. The

specimens were cooled after deformation with three different cooling rates of 1) 100℃/min, 2) 20℃/min, 3) 1℃/min, as shown in Figure 11.

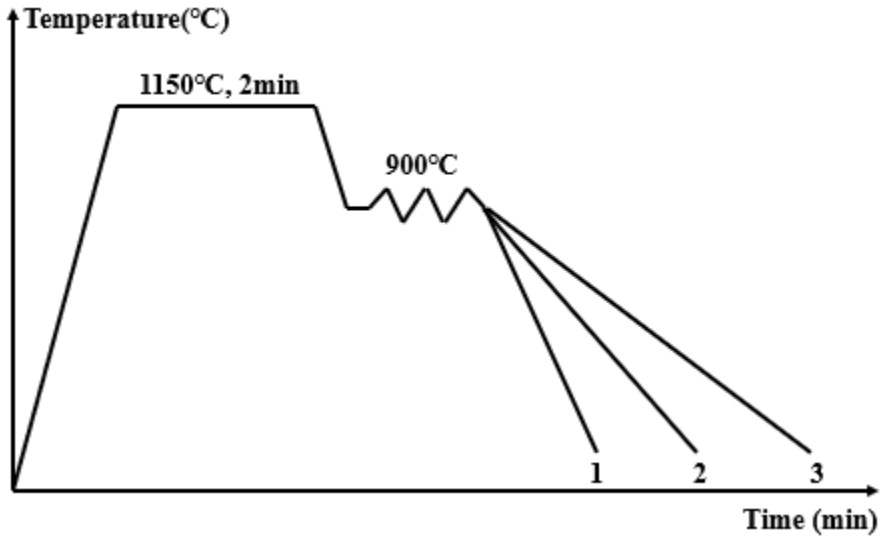

Figure 11 Schematic Representaion of Hot Deformation

The tests were performed using an INSTRON Universal Testing Machine adapted with an infrared furnace. To minimize oxidation, all the tests used Argon flow gas. Figure 12 shows the test equipment and conditions. The hot compression system has high strength at high temperatures WC dies. Prior to testing the dies are reheated to the deformation temperature using an infrared furnace, Chamb IR-E4-D-01-A, equipped with four lamps of 1000W, while the samples were preheated in a muffle furnace, from Thermolyne Thermo Scientific. The sample is then placed between the dies and immediately deformed. The samples will be subjected to continuous cooling after deformation.

Figure 12 Hot Deformation System

6.3.3 Microstructure Analysis

Samples were grinded with abrasive paper (320, 400, 600, 800 and 1200) and polished with a 0.05µm alumina suspension. To reveal the microstructure, all the samples were lightly etched with 3% Nital for 4 seconds. Optical microscopy was performed with the aid of a Keyence VHX-600 Digital Optical Microscope and SEM-FEG microscopy was performed using Zeiss Sigma500 VP equipped with Oxford Aztec X-EDS. The analysis of the microstructural features was performed using a 20KeV accelerating voltage in Secondary Electron mode.

To perform Electron Backscattered Diffraction (EBSD) and Image Quality (IQ) analyses, the samples were prepared using standard metallographic sample preparation. Additionally, vibratory polishing, using the GIGA-0900 metallographic system; samples were vibro polished for

180 minutes. These analyses were conducted on a FEI Scios DualBeam equipped with an EBSD camera, with an accelerating voltage of 20KeV, 13nA of beam current and a working distance of 14mm. All maps were recorded using a 0.2μm step size and an area of 100μm x 100μm under 1000X magnification. The information collected was processed using the TSL-OIM data analysis software. The color-coded map for the Inverse Pole Figure (IPF) was obtained in the Z-direction [001] with respect to the original deformation direction in the Wrought steel. While the building direction (Z-direction) was used for the IPF color map in the SLM steel. The EBSD scans for the WQ Wrought 4340 were done using the procedures described before, but with a larger (200μm x 200μm) scan area. The difference in the size of the areas scanned between the SLM and the Wrought steel was due to the difference in the refinement of the initial microstructures.

The as-reheated PAGS were revealed from the austenitic EBSD maps. The procedure was done with the aid of the MatLab software (R2018a for academic use, The Matworks Inc., Natick, MA, USA) and a MTEX toolbox [40, 41]. The threshold used to plot the PAGB was 3° misorientation.

Hardness measurements in all microstructural conditions were assessed with the aid of a Leco's AMH55 automated micro hardness testing system.

7.0 Result and Discussion

7.1 As-received Condition

Figure 13 exhibits the initial microstructure of both steels. The microstructure of SLM 4340 is composited by Martensite and Tempered Martensite due to the rapid solidification during deposition and high hardenability of 4340 steels. The subsequent deposited layers cause tempering of the previously deposited ones. The microstructure of the Wrought 4340 steel is Ferrite matrix with cementite and alloyed carbides.

Figure 14 shows OM and SEM images of non-metallic inclusions and oxides in Wrought 4340 and porosity observed in SLM 4340. The volume fraction of porosity in SLM 4340 measured by Archimedes' principle is less than 1%. At this level of microstructural analysis, the major difference between samples is the presence of coarse non-metallic inclusions and oxides in the Wrought 4340 and the presence of porosity in the SLM 4340.

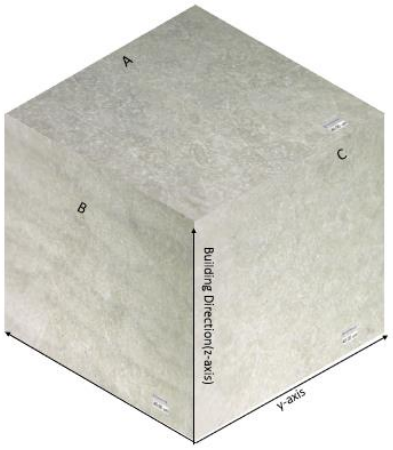

(a)

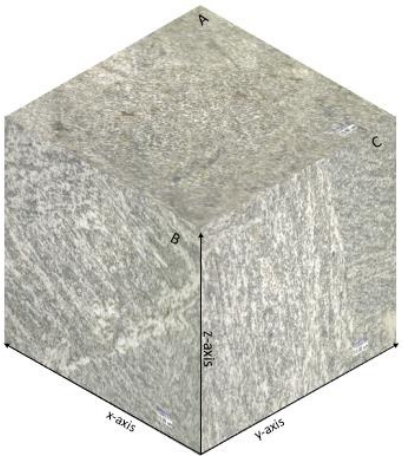

(b)

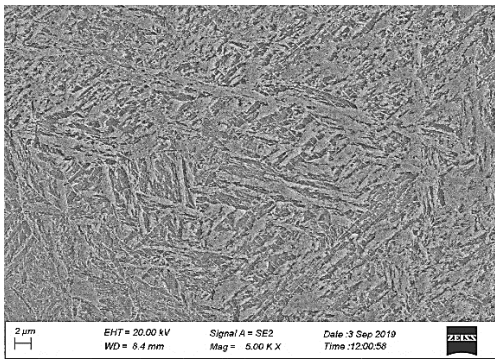

(c)

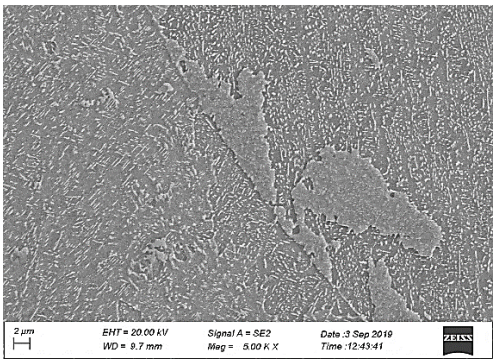

(d)

Figure 13 3D OM Images of SLM 4340 (a) and Wrought 4340 (b), SEM Images of SLM 4340 (c) and Wrought 4340 (d)

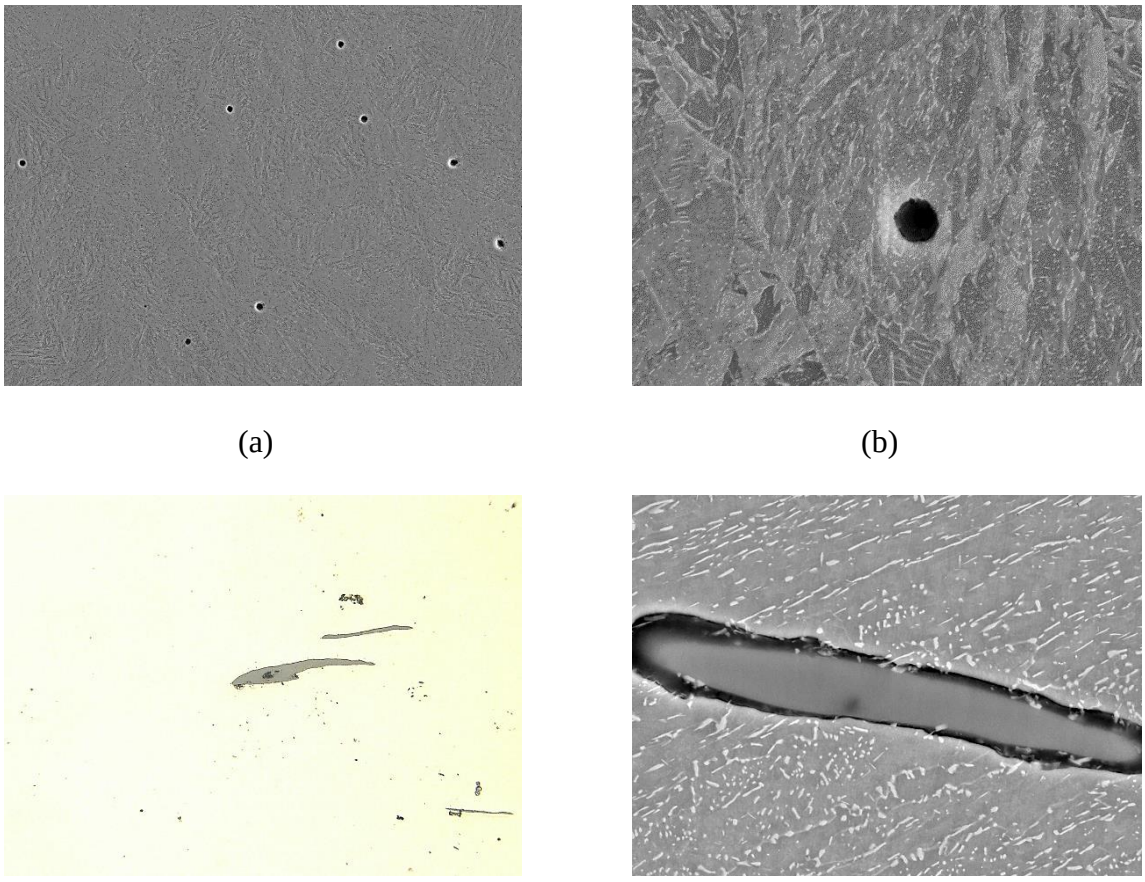

(a) (b)

(c) (d)

Figure 14 Porosity in SLM 4340 under SEM (a) and (b), and MnS inclusion in Wrought 4340 under (c) OM and (d) SEM

EBSD-IQ analysis are shown in Figure 15 and Figure 16. The principle of EBSD-IQ analysis is described in previous chapter. The result supports the prior microstructural description of the as-received samples.

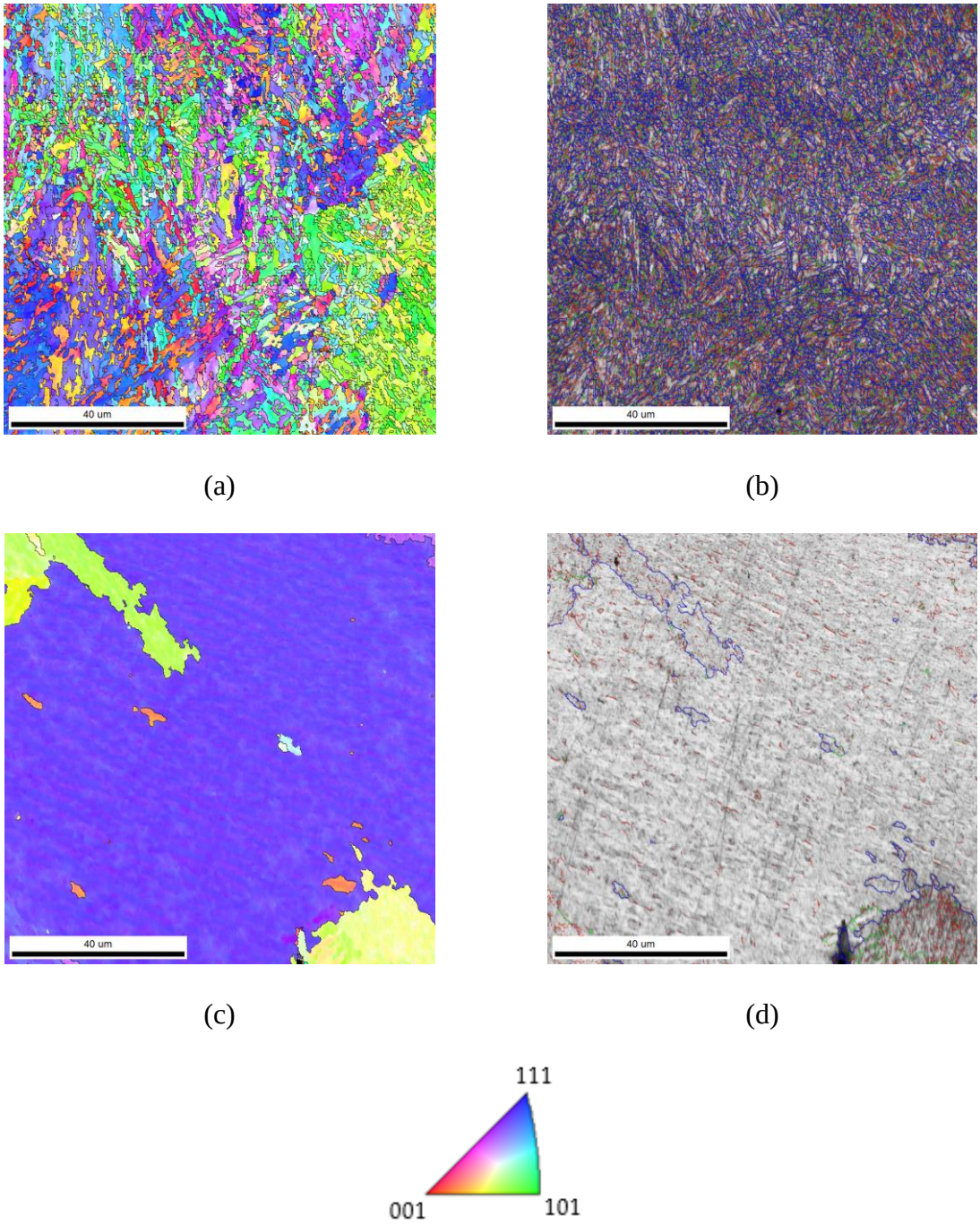

Figure 15 IPF Map of the (a) as-received SLM 4340, IQ map of the (b) as-received SLM 4340, IPF Map of (c) Wrought 4340 and IQ map of the (d) as-received Wrought 4340

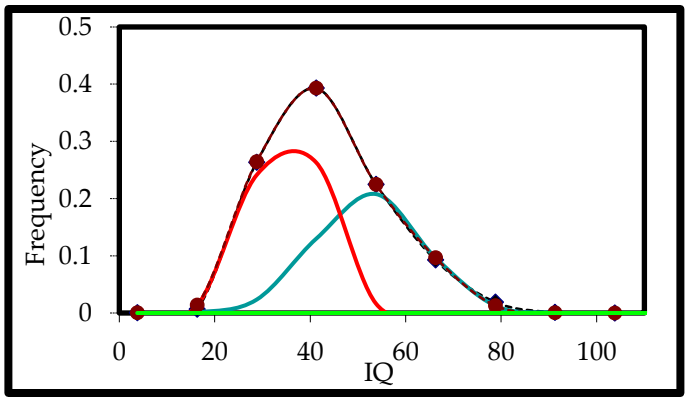

Martensite – 53.1%

Tempered Martensite – 46.9%

(a)

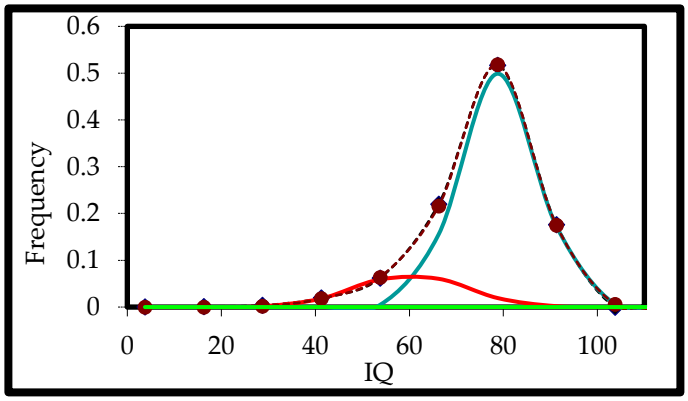

High Carbon (Alloyed) Carbides – 16.1%

Ferrite – 83.9%

(b)

Figure 16 EBSD-IQ Measurements for (a) as-received SLM 4340 and (b) as-received Wrought 4340

7.2 Austenite Grain Growth Behavior

The results from the Austenite grain coarsening studies are presented in Figure 17 and Figure 18. The Austenite grain size in the SLM steel samples did not show any significant grain coarsening up to the maximum reheating temperature of 1150°C used in this study. While the Austenite grains in the Wrought steel samples showed the traditional normal grain growth as the reheating temperature increases. To achieve reliable results, the sizes of 100 random grains were

measured and the average grain size value was determined. This process was repeated for all reheated conditions. Austenite grain size of Wrought 4340 is increasing homogeneous at low temperature because there are a great number of second-phase particles in the steel below 1150℃. These particles pin the austenite grain boundary and prevent the grain growth in heating process. When soaking temperature is above 1150℃, these particles are dissolved into austenite and grain grow rapidly.

SEM analysis of the Austenite grain boundaries in the SLM samples clearly showed the presence of porosity along triple points and along grain boundaries. The presence of porosity provided sufficient pinning force preventing the mobility of Austenite grain boundaries, hence inhibiting grain coarsening. Figure 19 shows an example of an Austenite grain after reheating at 1150℃ for 60 minutes and WQRT. The SEM micrograph illustrates the presence of pores located at the triple points and along the grain boundaries of Austenite.

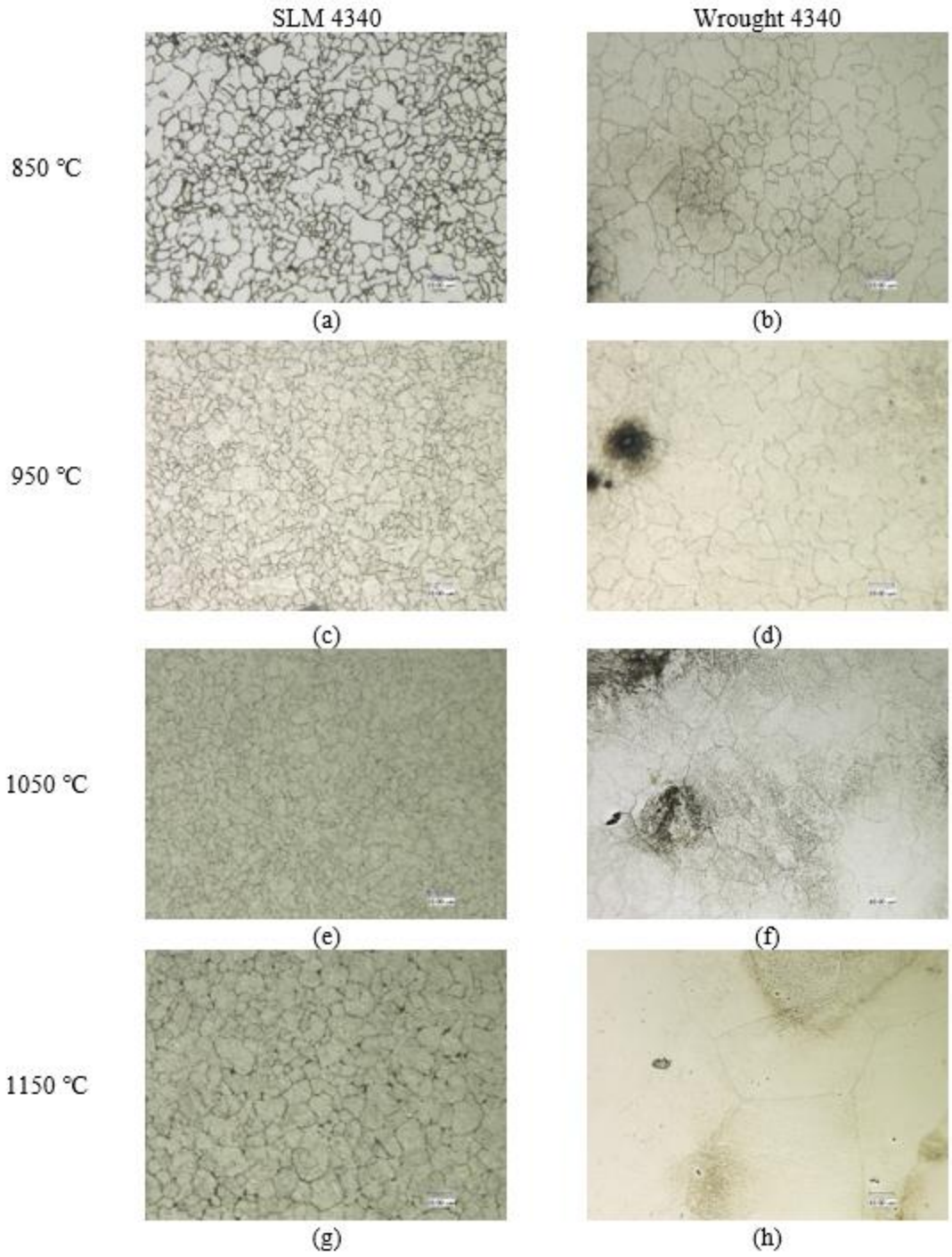

Figure 17 OM Images of PAG of SLM 4340 held at 850°C (a), 950°C (c), 1050°C (e), 1150°C (g). OM images of Wrought 4340 held at 850°C (b), 950°C (d), 1050°C (f), 1150°C (h)

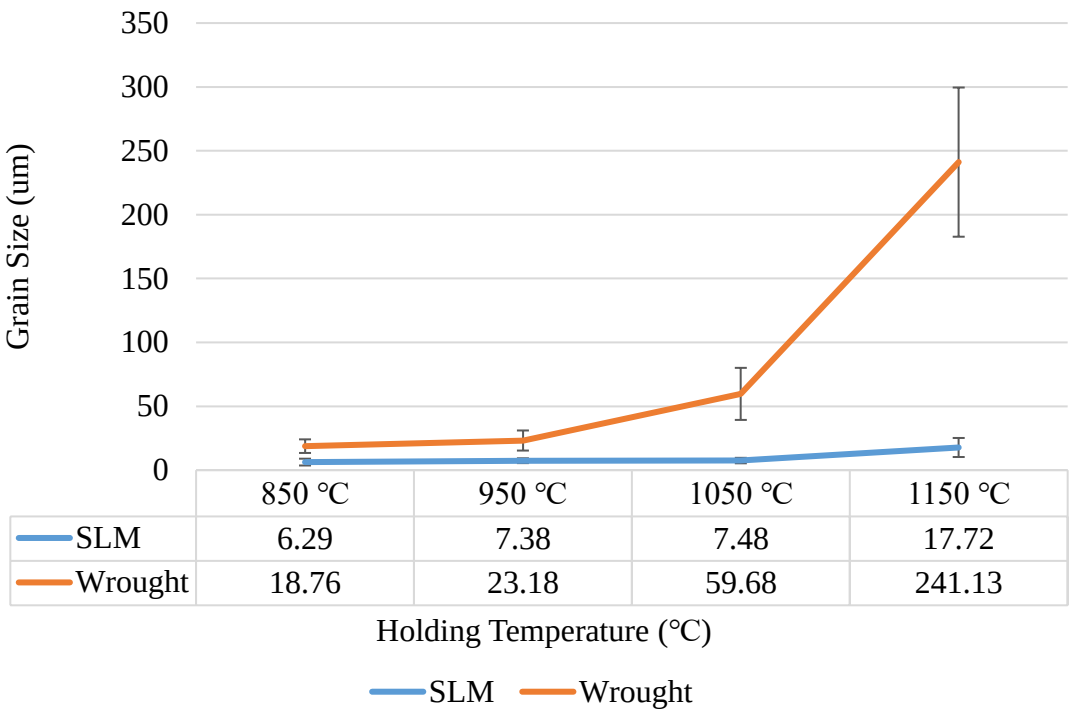

Figure 18 Comparasion of the Austenite Grain Coarsening Behavior between the Wrought and SLM steels

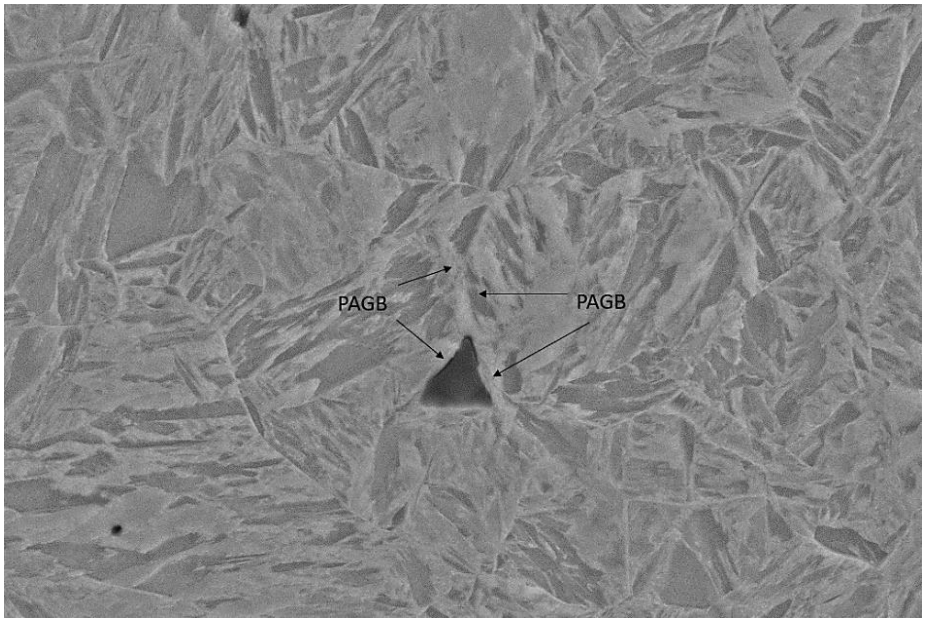

Figure 19 SEM showing the Prior Austenite Grain Size (PAGS) with Porosity at the Triple Points and along the γgb after Reheating at 1150℃ and WQ; etched with 3% Nital

This observation clearly suggests that the size and volume fraction of the pores in the SLM provides a pinning force (Fp) that is higher than the grain coarsening force (FGC). It is expected that as the reheating temperature increases the volume fraction of the pores will be reduced by the classical grain boundary and volume diffusion mechanisms; hence the Fp will be reduced. At this point the FGC > Fp and grain coarsening will start to take place.

Figure 20 shows the change in porosity and the austenite grain size as function of the reheating temperature for the SLM 4340. The porosity was measured by Archimedes' principle. It is clear that the percent of porosity decreases with the increasing of reheating temperature the grain boundary energy and mobility increase [42,43] and the Austenite grain boundaries start to grow. In summary, the presence of porosity provides the pinning mechanism inhibiting grain coarsening in the SLM steel.

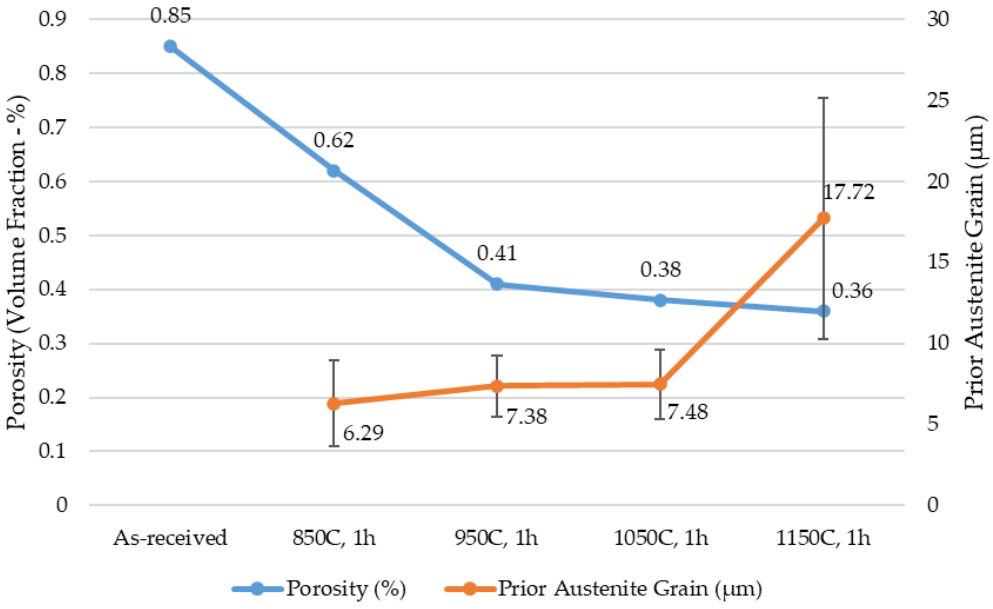

Figure 20 Change in Porosity and Austenite Grain Size as Function of Reheating Temperature for 4340 SLM steel

7.3 Continuous Cooling Transformation Behavior

It is well known that the transformation behavior of ferrous alloys during heating and/or cooling is associated with a significant contraction/expansion due to the volumetric changes of the crystal structure [44, 45]. These volumetric changes are observed by a change in the slope of the linear thermal expansion or contraction when a solid-solid phase transformation starts to take place. To analysis dilatometric curves correctly, differential curves were necessary [46]. This behavior was employed to construct the CCT diagrams for both steels, based on dilatometric curves see Figure 21.

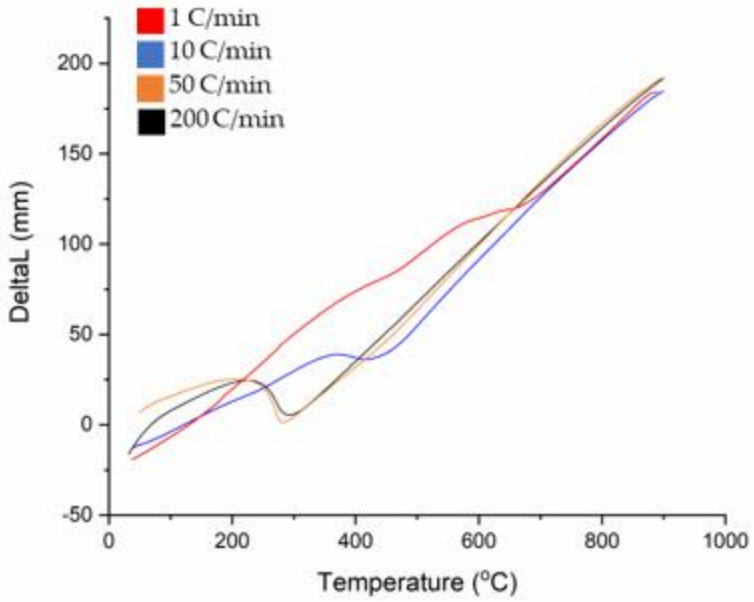

(a)

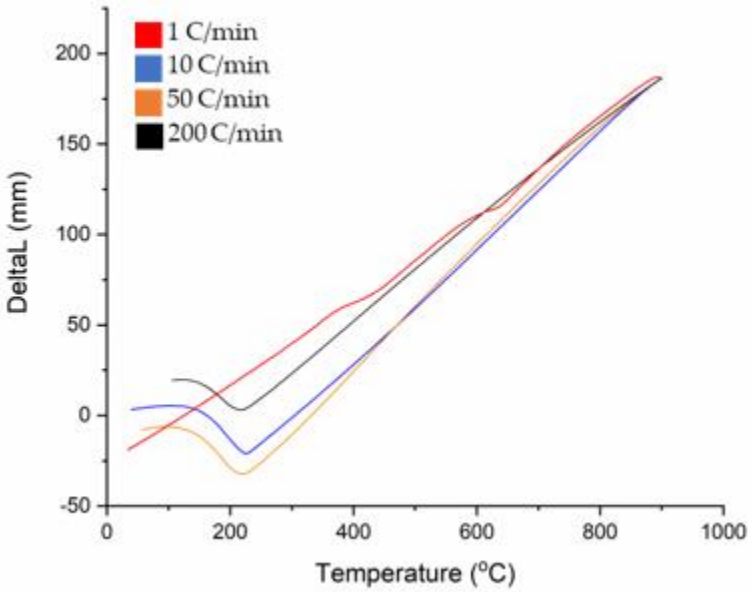

(b)

Figure 21 Dilatometric curves for (a) SLM 4340 and (b) Wrought 4340

7.3.1 Construction of CCT Diagram

Ac1 and Ac3 temperature are determined at a heating rate of 50C/min. Figure 22 and Figure 23 shows dilatometric curves and differential curves of Wrought 4340 and SLM 4340 during heating process.

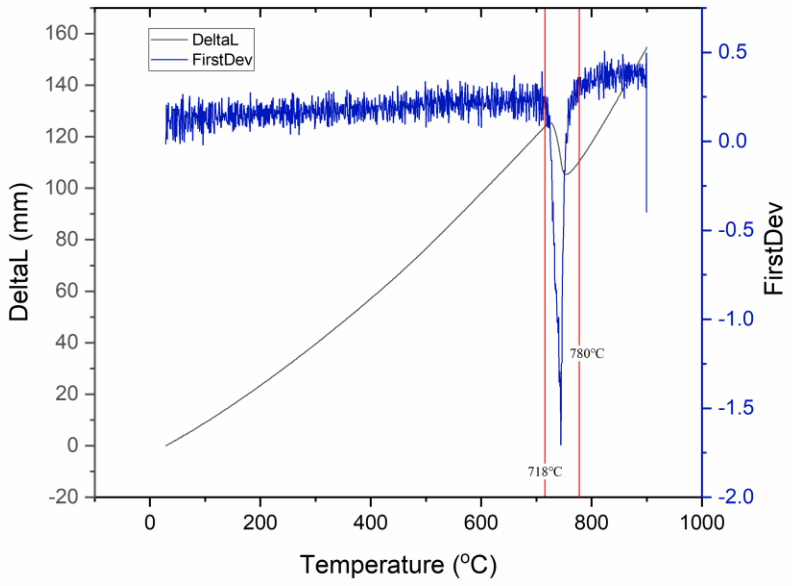

Figure 22 . Heating Dilatometric Curve with its Differential Curve for SLM 4340

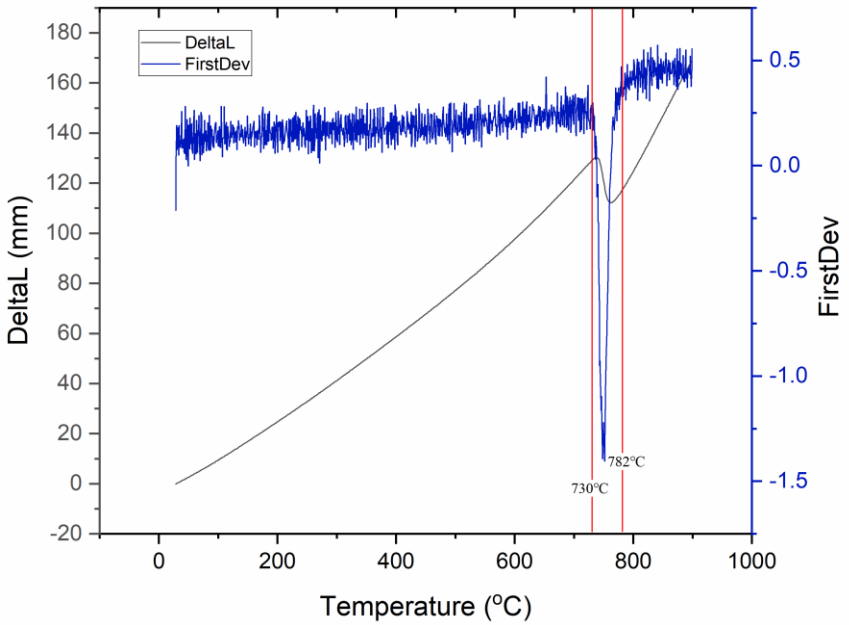

Figure 23 Heating Dilatometric Curves and its Differential Curves for Wrought 4340

The first deviation on dilatometric curves, which is equivalent to the start of the austenitic transformation, occurs at the temperature of 718C for SLM 4340 and 730℃ for Wrought 4340. As the heating continues, the first diffusion curve returns to a stable interval in a temperature of 780C for the SLM 4340 and 782℃ for the Wrought 4340, representing the end of this phase transformation, under this condition.

The dilatometric curves were processed in a similar way during cooling. The dilatometric and its first differential curves for the SLM 4340, cooled at 100℃/min, are shown in Figure 24. In this case, the length of the sample increased distinctly, and the diffusion curve varied significantly in the temperature range from 318℃ to 172℃. This observation can be combined with the microstructural analysis, confirming that the martensitic transformation has happened in this temperature range.

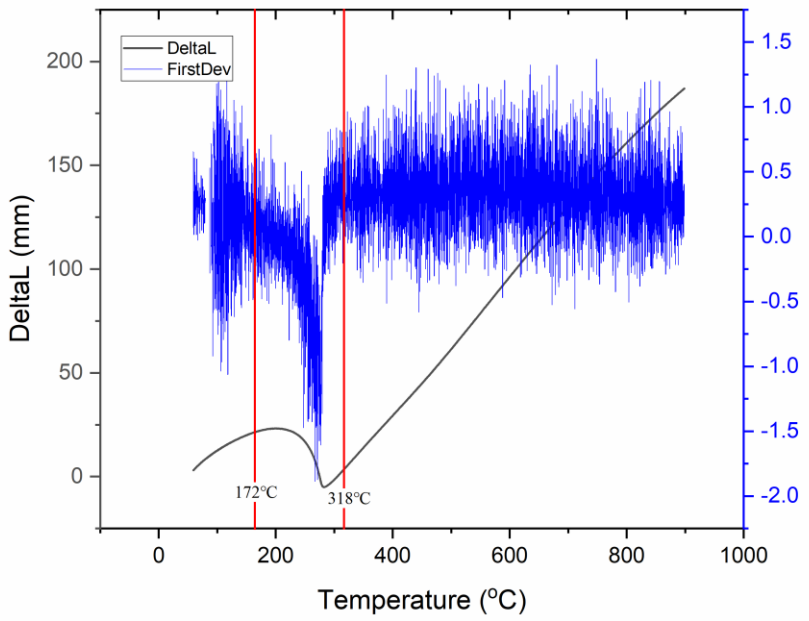

Figure 24 Cooling Dilatometric Curves at Cooling Rate of 100C/min for SLM 4340

Figure 25 shows the CCT diagram for the SLM 4340 steel, and Figure 26 shows it for the Wrought 4340 steel. Some important observations can be highlighted from the results. The hardenability of the Wrought 4340 steel is higher than that of the SLM 4340 steel. For example, in the Wrought 4340 steel, the Austenite (γ) → Bainite (B) field is pushed to the right and at lower transformation temperatures compared to the SLM steel. One plausible explanation is that the presence of porosity reduces the stability of Austenite and shortens the nucleation time of the Austenite transformation [47].

The Granular Bainite in the Wrought 4340 could only observed in cooling rate lower than 1°C/min. In SLM 4340, GB is detected in cooling rate up to 20°C/min. The presence of Granular Bainite in these materials are not reported in open literature. These microstructural features will be shown in the microstructural section. This observation is important because during the

decomposition of Austenite no major changes in the linearity of the time-temperature behavior were associated with GB or MA.

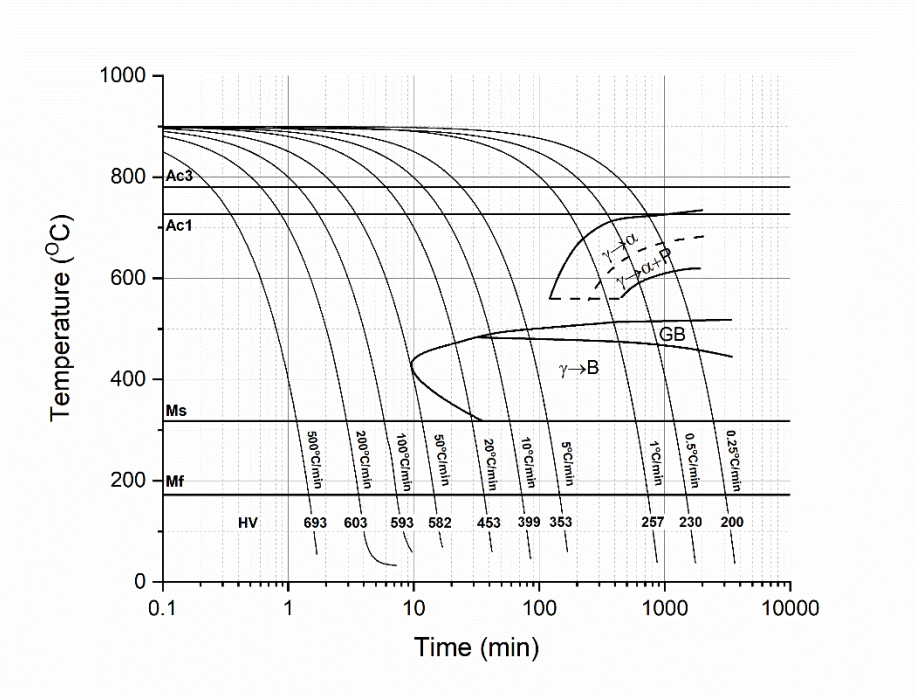

Figure 25 Constructed CCT Diagram for SLM 4340 Steel

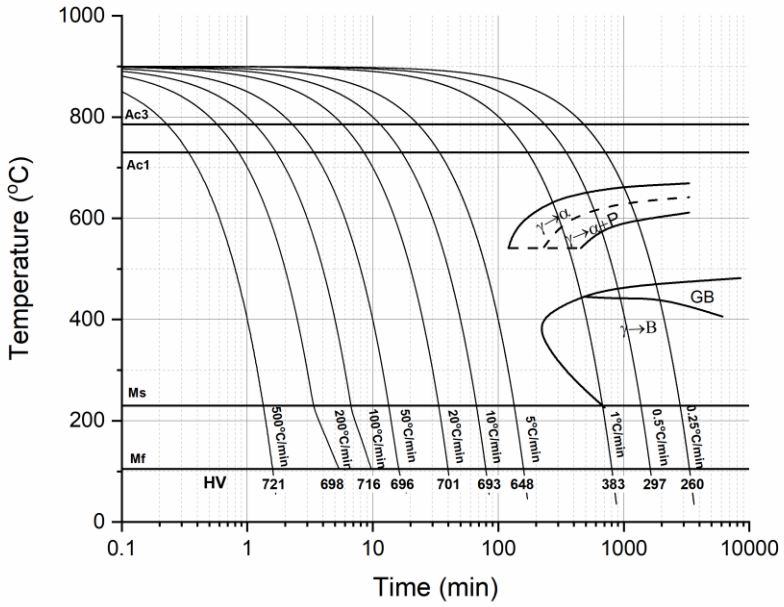

Figure 26 Constructed CCT Diagram for Wrought 4340 Steel

Figure 27 shows the average bulk micro hardness (HVN) values attained. These measurements were performed to assess the impact of different cooling rates on the resulting microstructures. The HVN results indicated that the microstructures obtained from the Wrought 4340 steel were harder than those from the SLM steel for a given cooling rate. The hardness results can be rationalized in terms of the microstructural conditions of the Austenite grain size and its chemical composition prior to its transformation. In this thesis, just the effect of microstructural condition is discussed.

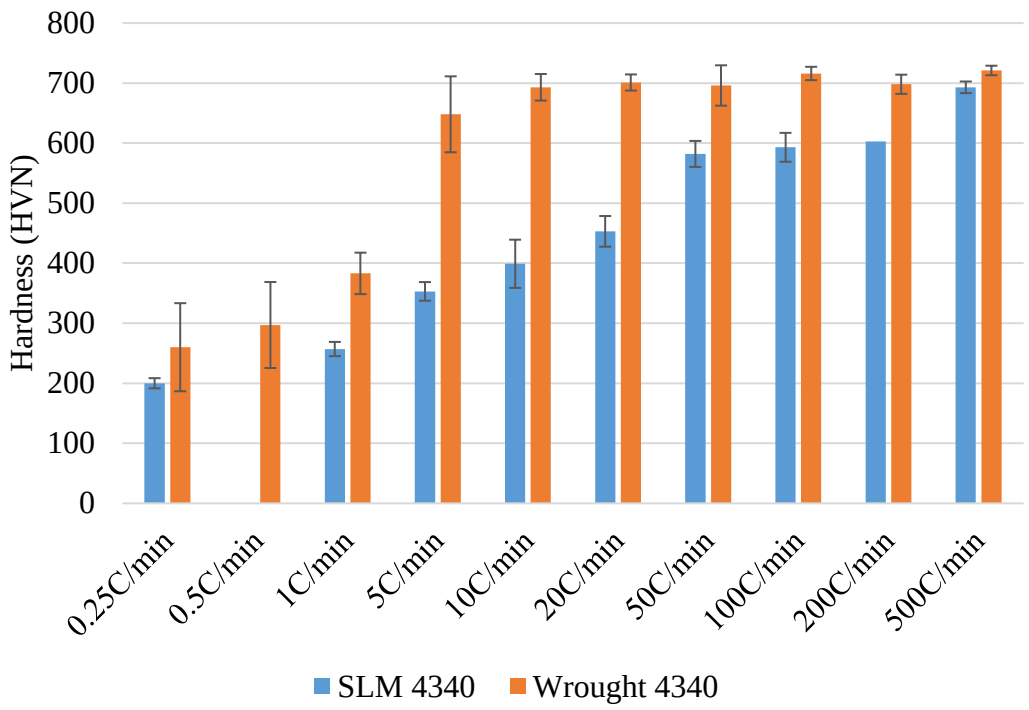

Figure 27 Average Bulk Hardness Values for SLM 4340 and Wrought 4340 steels

7.3.2 Microstructure Analysis

7.3.2.1 SLM 4340

The transformation behavior of Austenite under uniform continuous cooling paths provided a wealth of microstructural information. For example, at the slowest cooling rate, i.e. 0.25°C/min, the microstructure consisted of Ferrite-Pearlite with Cr-carbides along the grain boundaries. As the cooling rate was increased, other low temperature transformation products were observed. These were Martensite-Austenite (MA) and Granular Bainite, along the prior Austenite grain boundaries. At cooling rates between 50°C/min and 100°C/min, Bainite, Martensite and Carbides Free Bainitic-Ferrite were observed. Figure 28 shows examples of the typical SEM microstructures identified.

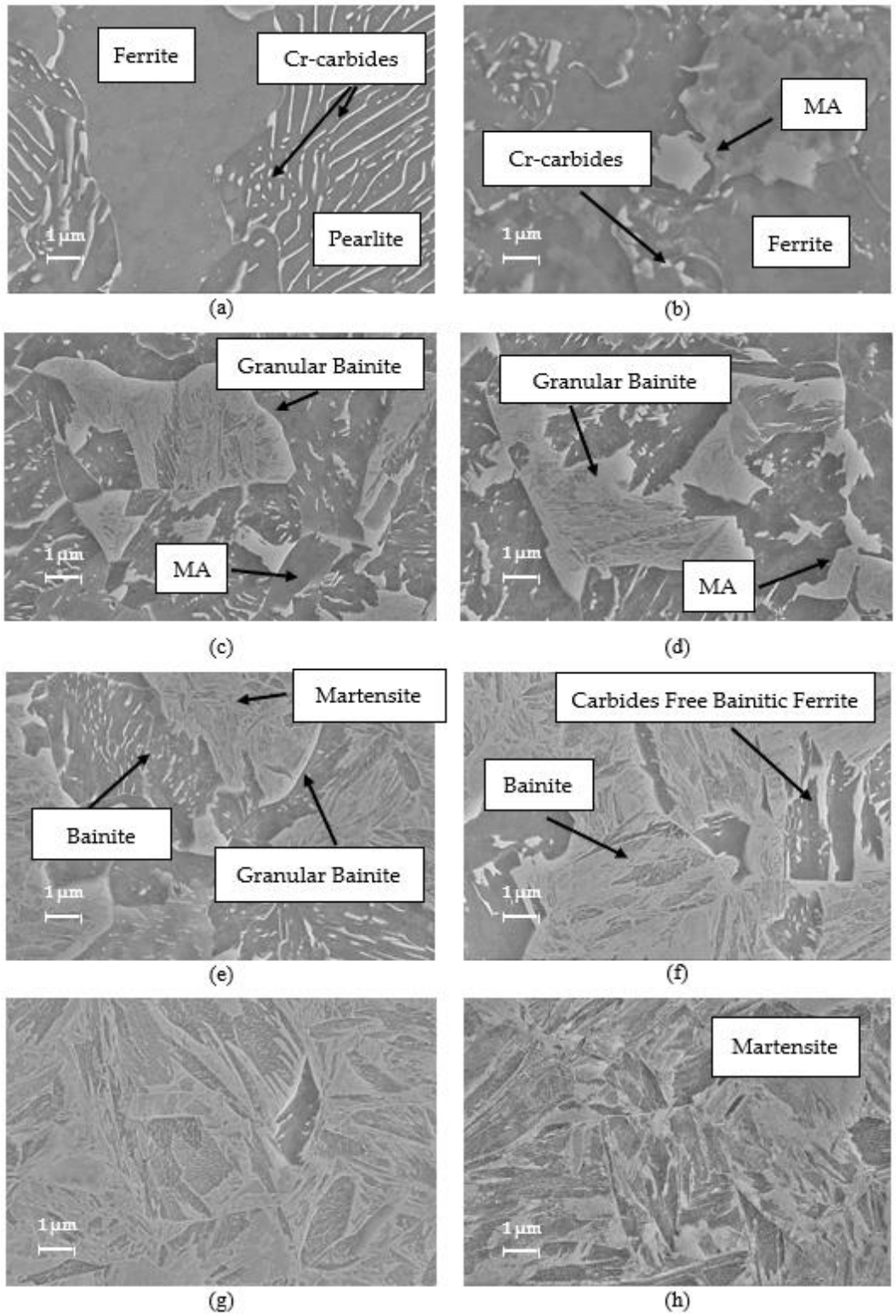

Figure 28 SEM of SLM 4340 (a) 0.25°C/min, (b) 1°C/min, (c) 5°C/min, (d) 10°C/min, (e) 20°C/min, (f) 50°C/min, (g) 100°C/min, (h) 500°C/min. All samples are etched with 3% Nital

7.3.2.2 Wrought 4340

The SEM microstructural analysis of the Wrought 4340 samples after uniform continuous cooling showed a substantially more complex microstructural distribution compared to the microstructures observed in the SLM samples. At slower cooling rates, i.e. 0.25℃/min, 0.5℃/min and 1℃/min, the microstructures consisted of Ferrite-Pearlite, Martensite-Austenite (MA) and Granular Bainite (GB). At higher cooling rates (≥ 5C/min) the main microstructural components were Bainite and Martensite.

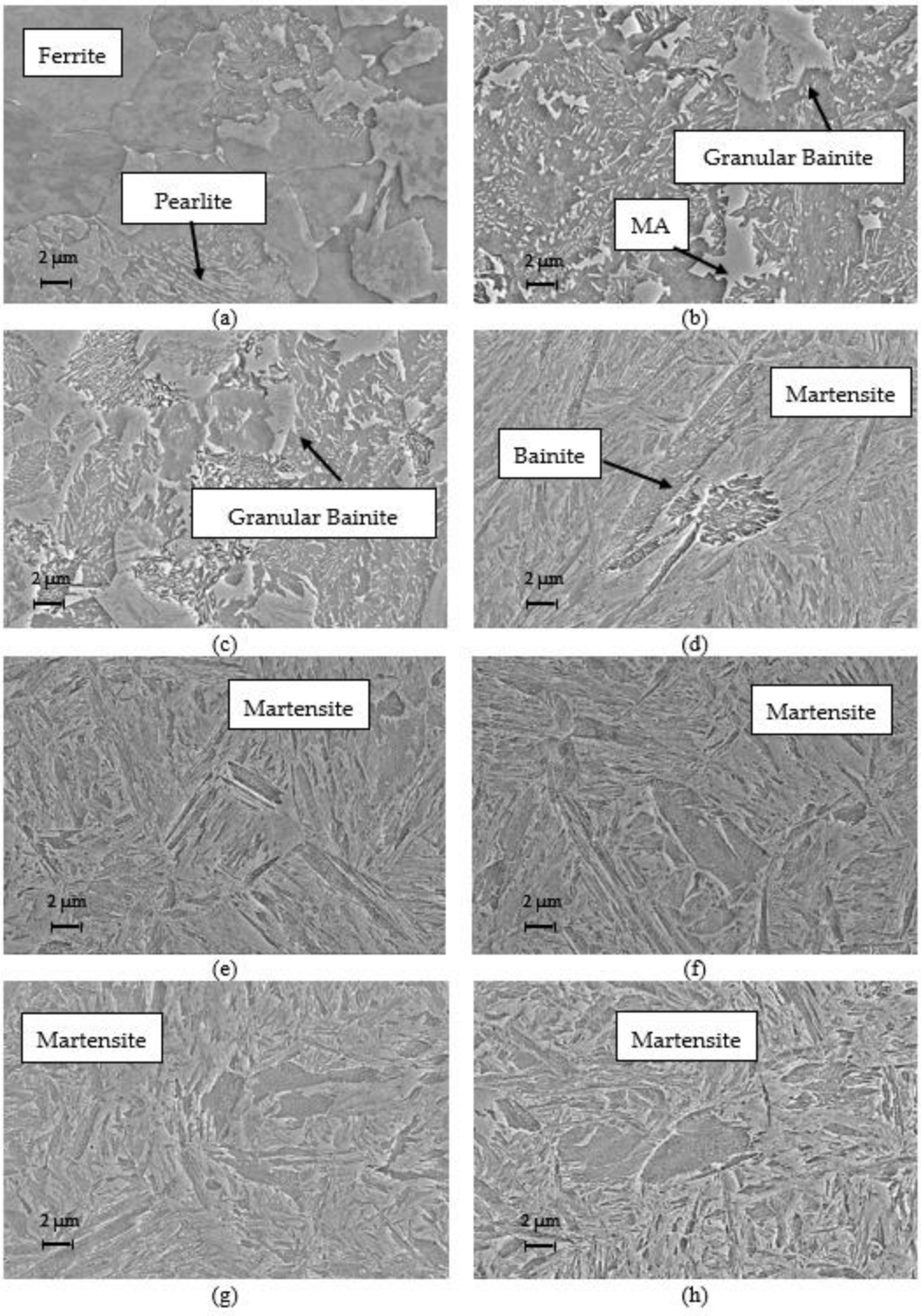

Figure 29 SEM pictures of (a) 0.25°C/min, (b) 0.5°C/min, (c) 1°C/min, (d) 5°C/min, (e) 10°C/min, (f) 20°C/min, (g) 50°C/min, all samples were etched with 3% Nital

7.3.3 Advanced Microstructure Analysis

7.3.3.1 SLM 4340

The reheated conditions were also analyzed and the reconstructed microstructures based on EBSD measurements and on EBSD-IQ for SLM 4340 are shown on Figure 30. Figure 30a shows the Inverse Pole Figure (IPF), Figure 30b, the IQ map and Figure 30c, a MatLab figure showing the IQ map in a colored scale, all for the cooling rate of 0.25°C/min, Figure 30 from (d) to (f) show the same for the cooling rate of 500°C/min.

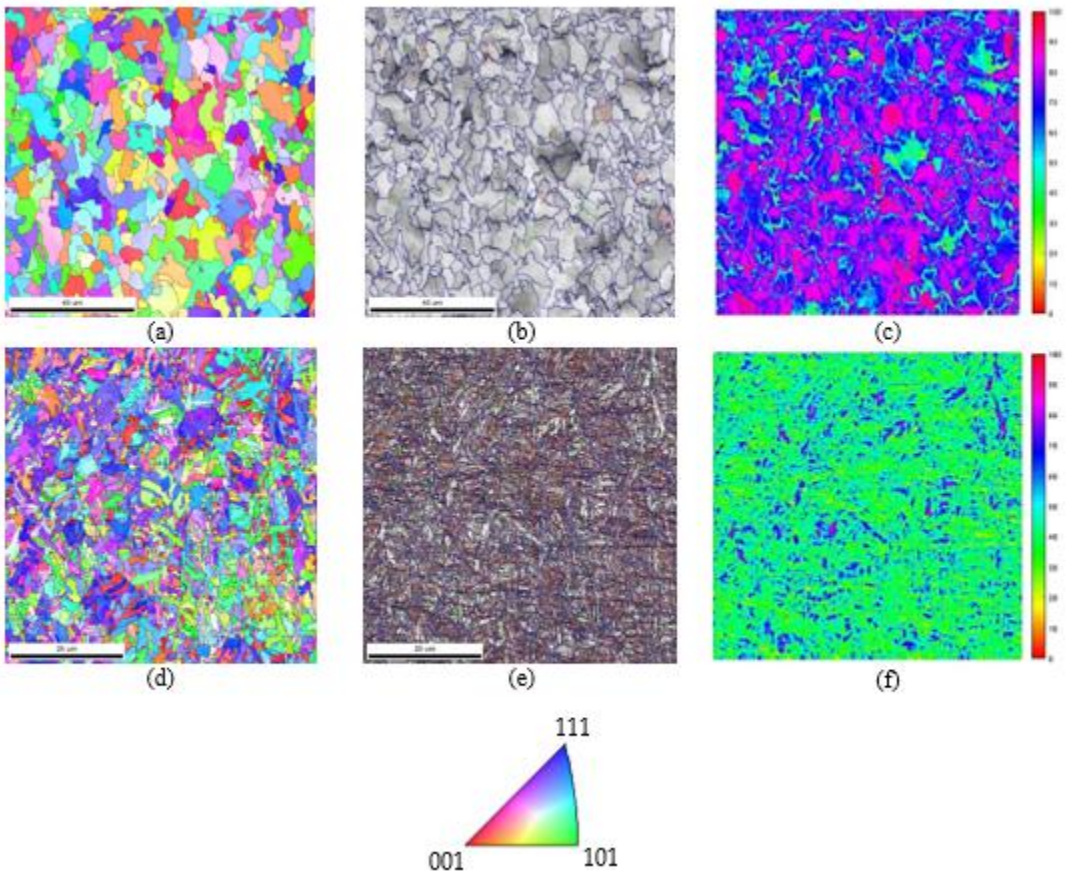

Figure 30 Reconstructed microstructures and EBSD-IQ for SLM 4340 cooled at (a, b and c) 0.25°C/min and (d, e and f) 500C/min

The color scale in Figure 30c and Figure 30f shows the micro-constituents that have lower dislocation density hence higher IQ values represented by purple and blue colors, while micro-constituents with higher dislocation density and lower IQs are shown by the green and yellow colors.

Figure 31 shows the EBSD-IQ phase balance for the SLM samples after cooling at 0.25℃/min and 500℃/min. The difference in the microstructural components supports the CCT and SEM results.

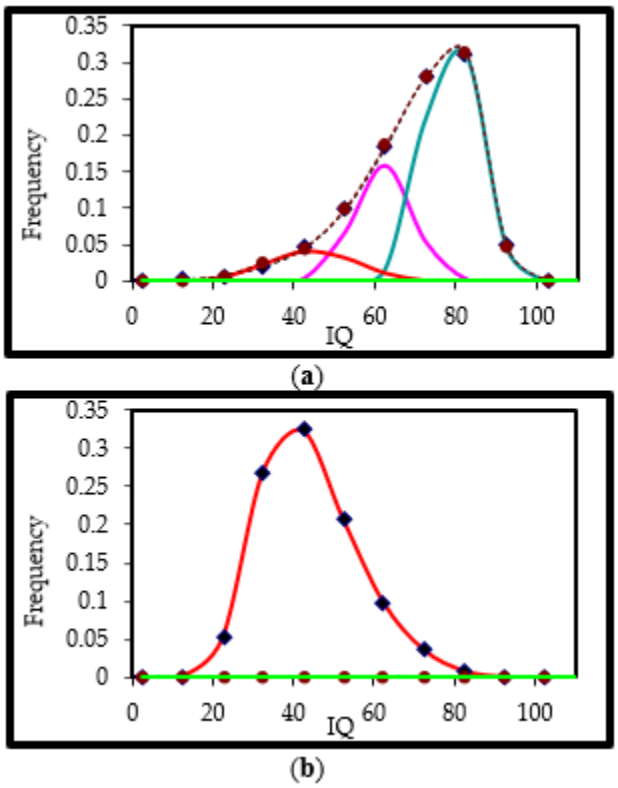

Cr-C-rich Constituents – 11.9%
Pearlite – 28.3%
Ferrite – 59.8%

Martensite – 100%

Figure 31 . EBSD-IQ Measurements for SLM 4340 cooled at (a) 0.25C/min and (b) 500C/min

The grain boundary character distribution (GBCD) in terms of low angle grain boundaries (LAGB), high angle grain boundaries (HAGB) and coincidence site lattice (CSL) boundaries are shown in Figure 32. As expected, the results clearly indicate that at the slower cooling rates most

of the grain boundaries were HAGB, as the cooling rate increased the GBCD became more uniform between LAGB, HAGB and CSL boundaries.

This behavior is strongly related to the nature of the transformation mechanisms and final microstructures during the decomposition of Austenite. That is, the GBCD for samples cooled at 0.25°C/min, 1°C/min have a higher percentage of HAGB when compared with LAGB due to the absence of low transformation products. At higher cooling rates the volume fraction of LAGB increased due to the formation of low temperature transformation products, i.e. Martensite and/or Bainite.

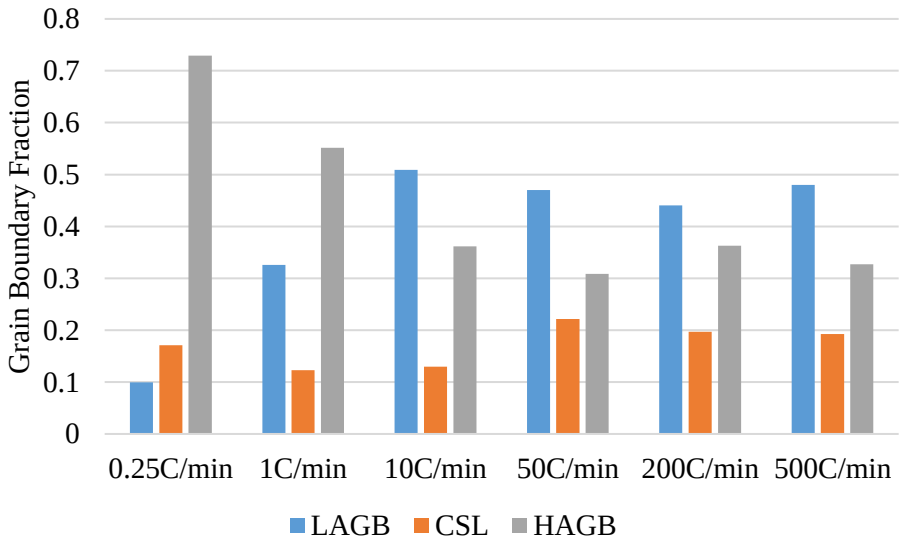

Figure 32 Grain Boundary Character Distribution for the SLM 4340

7.3.3.2 Wrought 4340

For the Wrought 4340, the reconstructed microstructures based on EBSD measurements are shown in Figure 33, while the EBSD-IQ results are shown in Figure 34. Figure 33a shows the

Inverse Pole Figure (IPF), Figure 33b, the IQ map and Figure 33c, a MatLab figure showing the IQ map in a colored scale, all for the cooling rate of 0.25℃/min. Figure 33 from (d) to (f) show the same for the cooling rate of 500℃/min. The color scale on Figure 33c and Figure 33f also shows the micro-constituents that have lower dislocation density hence higher IQ values by purple and blue colors, while phases with higher dislocation density and lower IQs are shown by the green and yellow colors.

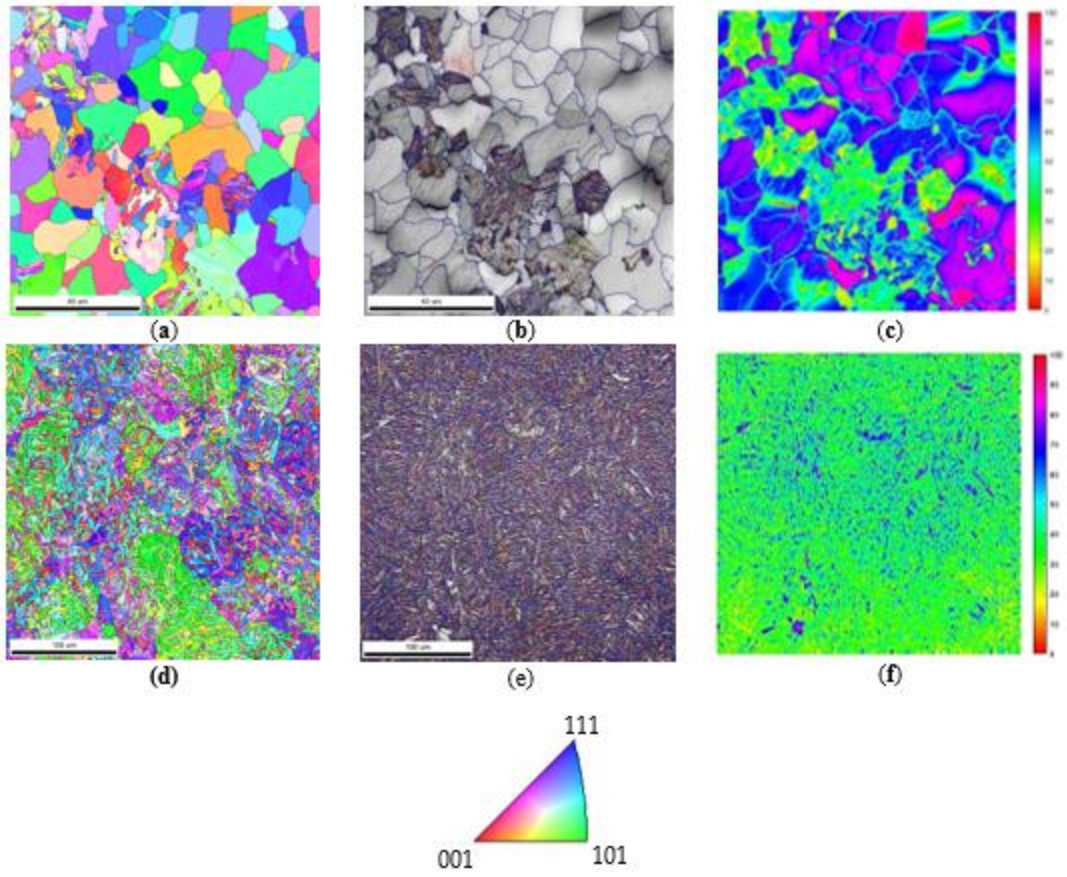

Figure 33 Reconstructed Microstructures and EBSD-IQ for Wrought 4340 cooled at (a, b and c) 0.25C/min and (d, e and f) 500 °C/min

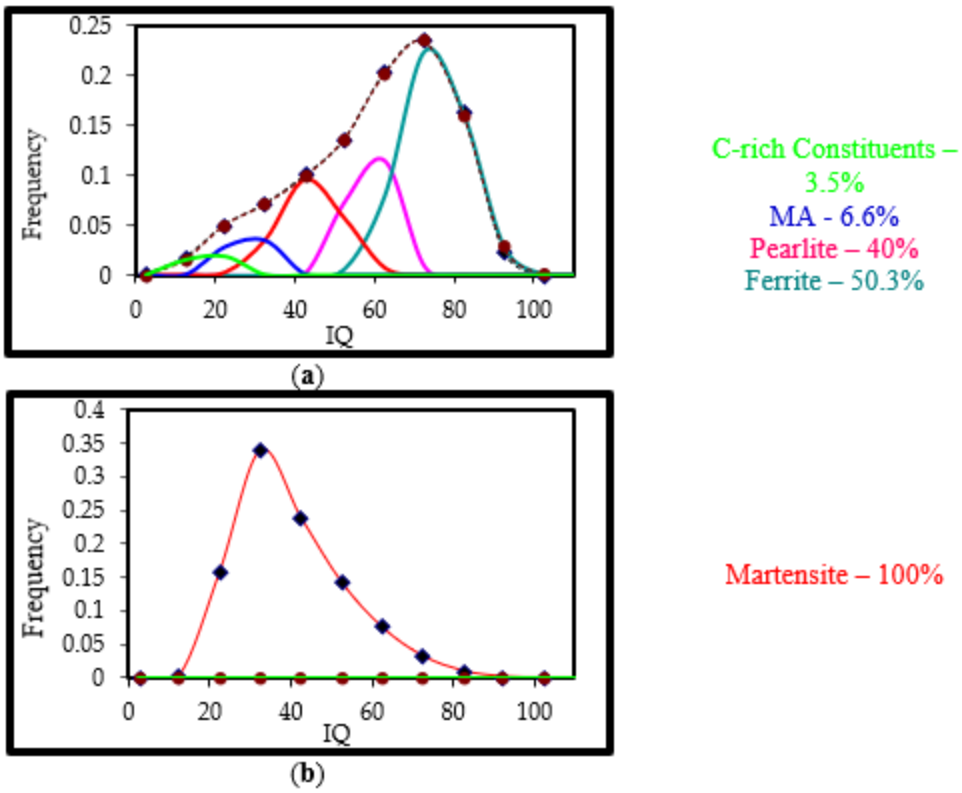

Figure 34 EBSD-IQ Measurements for Wrought 4340 cooled at (a) 0.25C/min and (b) 500C/min

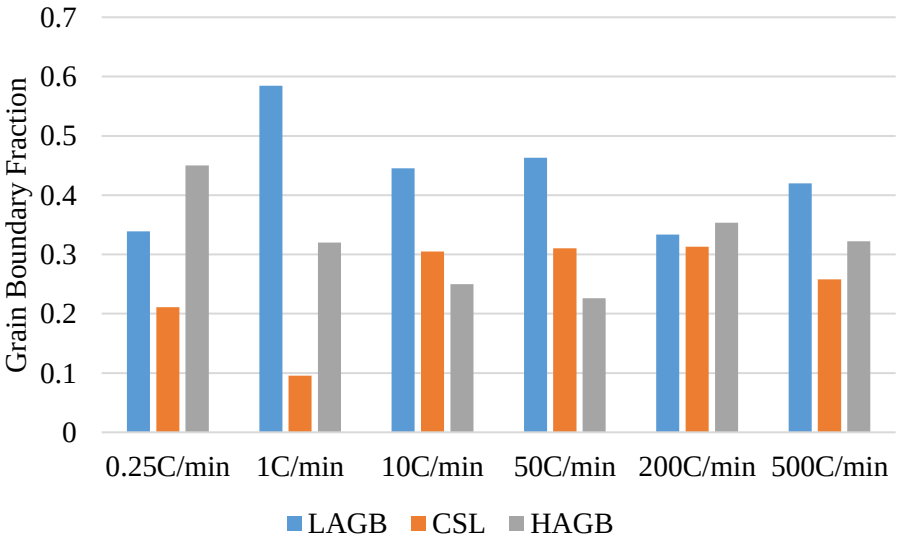

Figure 35 Grain Boundary Character Distribution for Wrought 4340

A comparison of the GBCD between the Wrought steel samples (Figure 35) to those from the SLM (Figure 32) reveals the presence of higher volume fraction of LAGB in the Wrought steel at low cooling rates. This supports the observations that the Wrought steel has higher hardenability than the SLM steel under the experimental conditions used in this study. As the cooling rate increases the GBCD balance becomes very similar for both steels.

7.3.4 Reconstruction of Prior Austenite Grain Boundary

The reconstruction of the PAGS from the Martensitic structures, using the MTEX technique 15-16 is displayed in Figure 36. Figure 36 from (a) to (c) compare the PAGS corresponding to the SLM 4340 and from (d) to (f) for to the Wrought 4340. All the reconstructed PAGS maps were performed based on the Inverse Pole Figure Maps (IPF) for each condition.

A comparison of the PAGS clearly shows two major points: 1) the SLM steel samples have finer Austenite grains compared to the Wrought steel samples; and 2) the average grain size distribution is also thinner in the SLM samples compared to the Wrought samples.

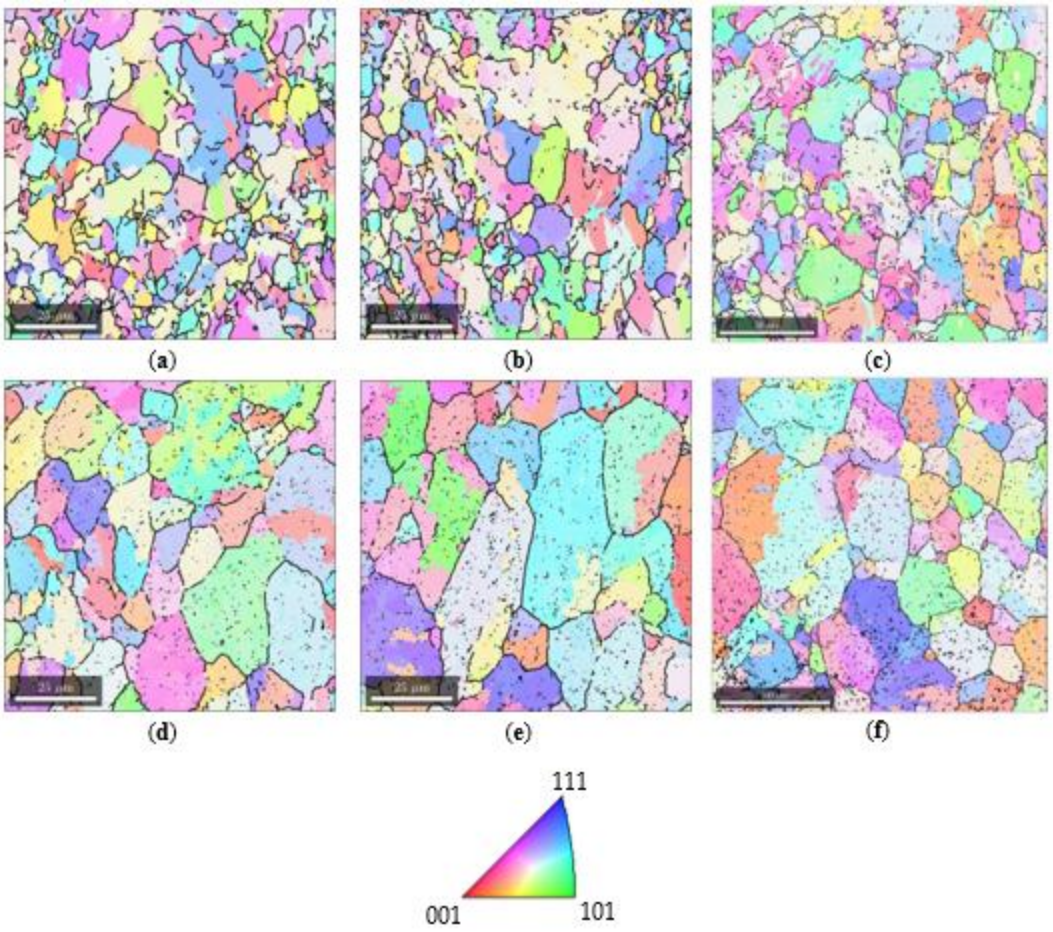

Figure 36 PAG Reconstruction for (a) 10C/min – SLM 4340, (b) 50C/min – SLM 4340, (c) 500C/min – SLM 4340, (d) 10C/min – Wrought 4340, (e) 50C/min – Wrought 4340 and (f) 500C/min – Wrought 4340

7.4 Hot Deformation Characteristics

The significant change of the austenite-ferrite transformation behavior from unrecrystallized austenite is well documented [47-51] Strain energy caused by hot deformation is the driving force of recrystallization, recovery, and phase transformation. Also, elongated grains and deformation band caused by deformation provide nucleation site for formation of ferrite. In this part, and nucleation site will be quantified by effective interfacial area per unit volume. The effect of cooling rate on transformation behavior from deformed austenite is also discussed in this part.

7.4.1 Effect of Hot Deformation on γ structure and Sv value

Depends on the hot deformation temperature, the austenite structure after deformation could be divided into fully recrystallized, partially recrystallized, and unrecrystallized. In this study, the form of austenite obtained by quenching is close to unrecrystallized. In both SLM and Wrought 4340 steel, elongated grains and deformation bands within the grain are observed, and phase transformation happen at these interfaces. The nucleation energy at grain boundaries is less than inside the grain, which means grain boundaries are favored sites for nucleation [52]. As mentioned in the Literature Review section, the increase of nucleation sites for the γ-α transformation depends on the amount of deformation in non-recrystallization region, expressed by effective interfacial area per unit volume (Sv).

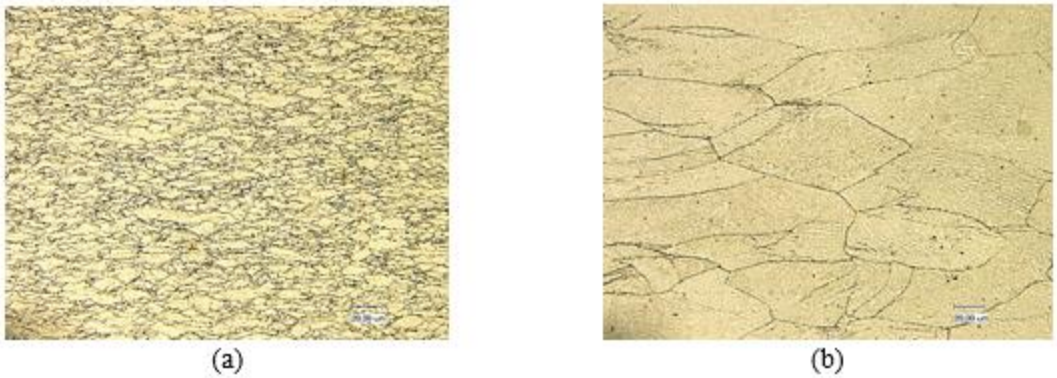

Figure 37 OM (1kX mag) showing the PAGB for (a) SLM 4340, and (b) wrought 4340 after deformation

Based on the knowledge above. The Sv value of both SLM and Wrought 4340 are shown in Figure 38, higher Sv value indicates more nucleation site for phase transformation, and result in finer microstructure. The Sv value of SLM 4340 is significantly higher than wrought 4340 both before and after hot deformation, which means SLM 4340 will have finer final microstructure.

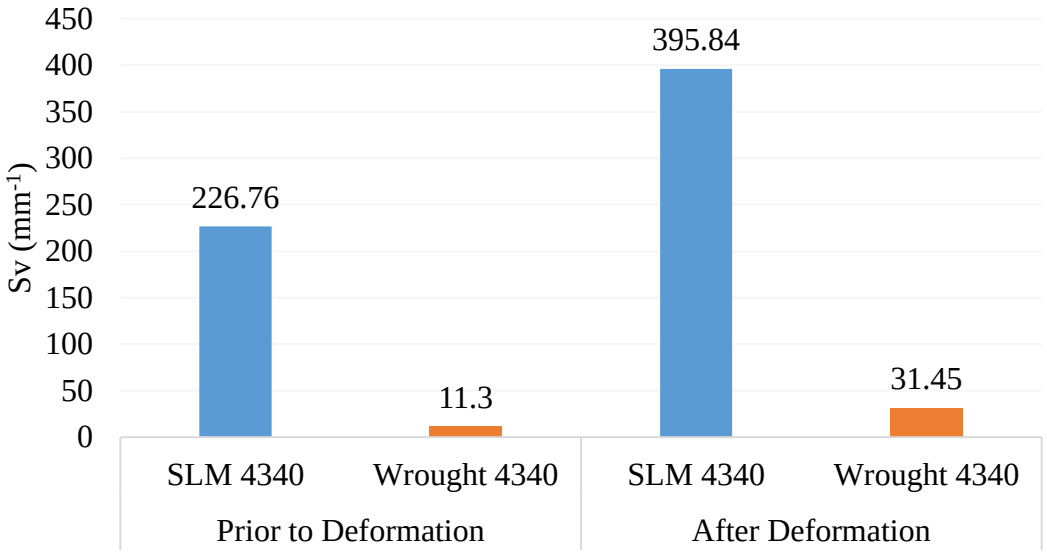

Figure 38 Sv Measurements for both alloys

7.4.2 The Effect of Cooling Rate on Transformation Behavior from Deformed Austenite

The transformation behavior of deformed austenite under continuous cooling conditions provided a wealth of microstructural information. The results from the microstructural characterization of the 4340 SLM and 4340 wrought samples will be described in the following sections. The results showed differences in terms of microstructural constituents, phase character distribution and micro-hardness values.

For the SLM 4340 sample, cooled at 1°C/min after deformation exhibited a ferrite-pearlite microstructure with Cr-carbides along the grain boundaries and a martensite-austenite (MA) phase. With the increase of the cooling rate, the microstructural components for the SLM sample cooled at 20°C/min were martensite, bainite, granular bainite (GB) and martensite-austenite (MA) and, for the SLM sample cooled at 100°C/min, the components were martensite, bainite and carbides-free bainitic ferrite. A martensitic phase distribution was observed for Water Quench sample. Figure 39 shows the SEM micrographs for the SLM 4340 steel. Due to close chemical composition, wrought 4340 has similar transformation behavior with coarser microstructure as shown in Figure 40.

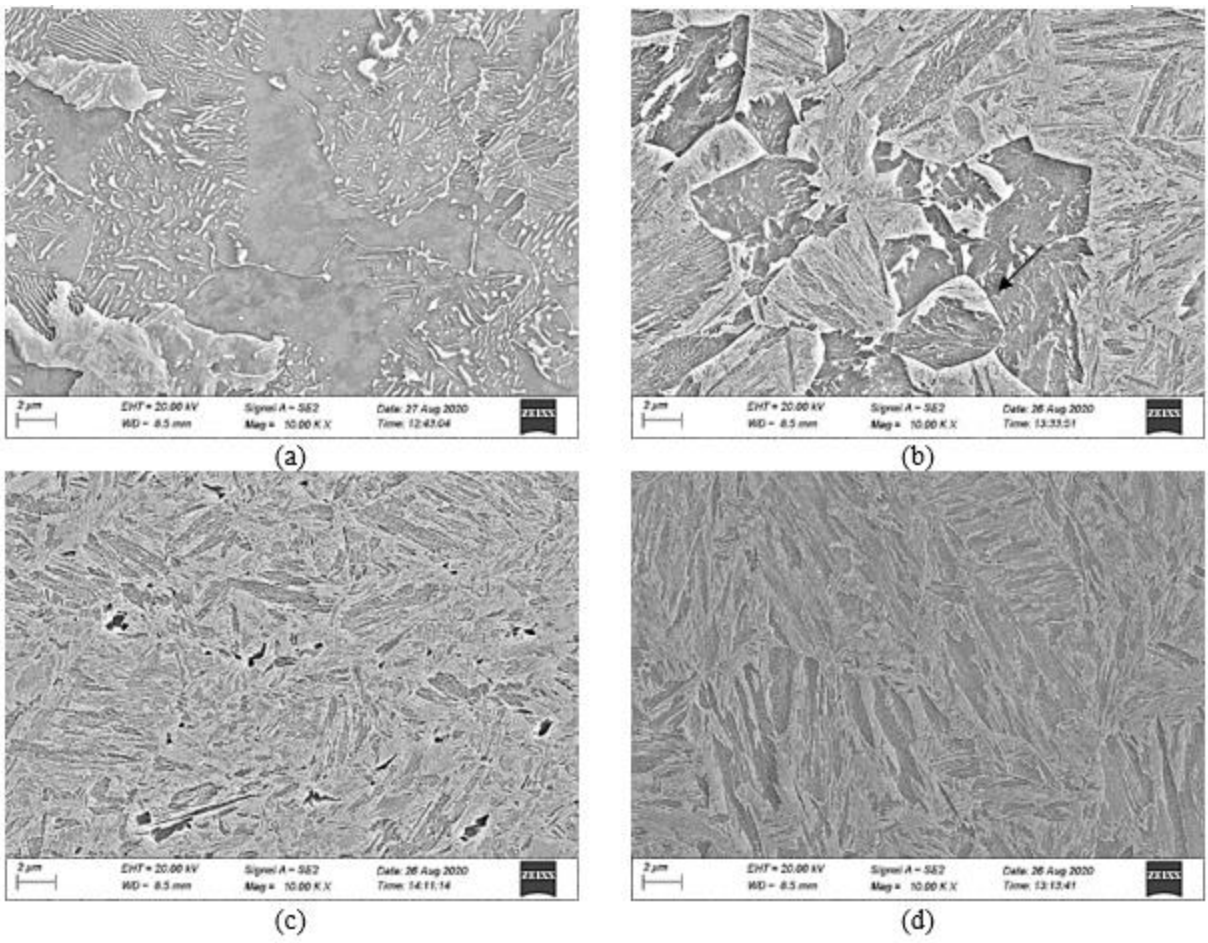

Figure 39 SEM micrographs (10kX mag) for the SLM 4340 cooled at (a) 1°C/min, (b) 20°C/min, (c) 100°C/min. (d) WQ after deformation

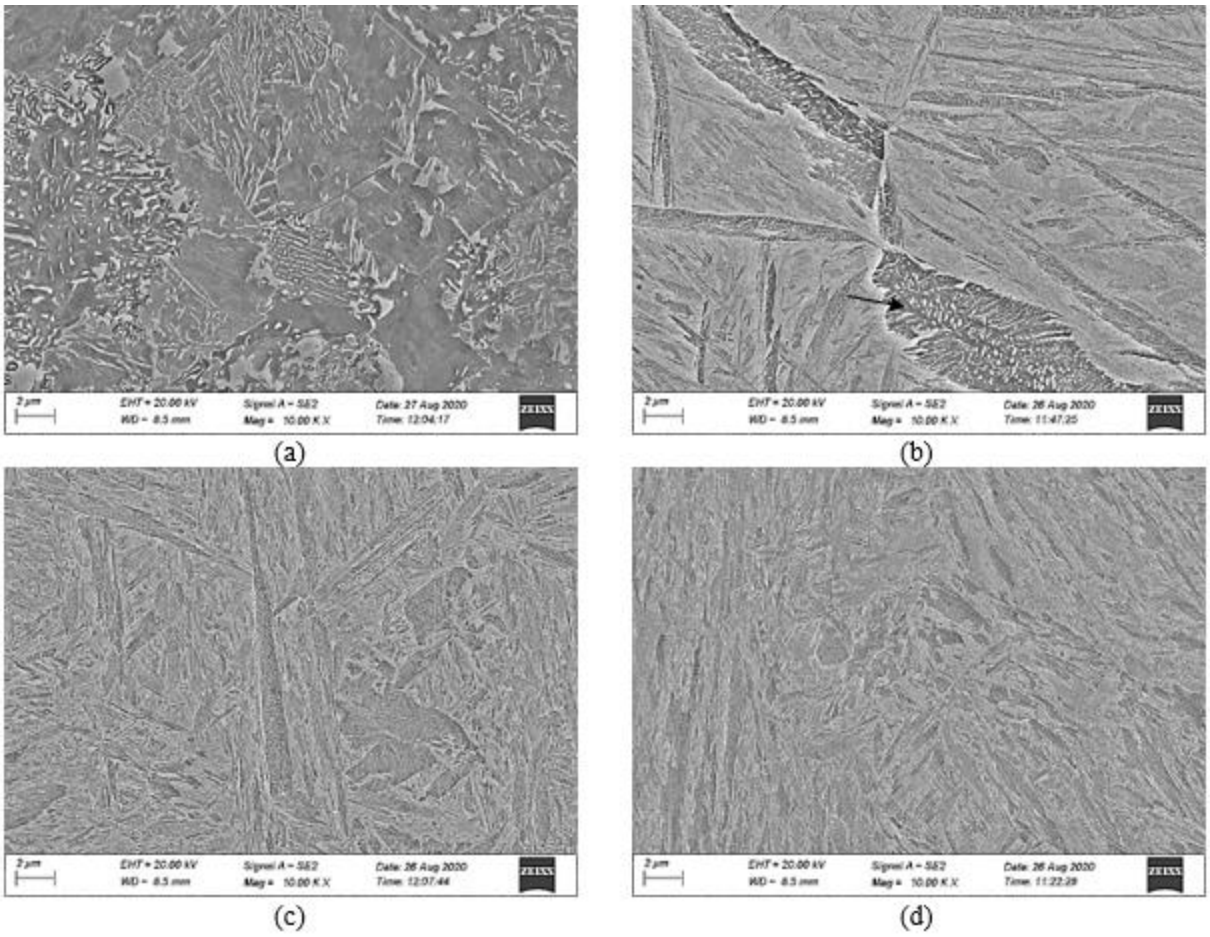

Figure 40 SEM (10kX mag) for the Wrought 4340 cooled at (a) 1°C/min, (b) 20°C/min, (c) 100°C/min. (d) WQ after deformation

A comparison of the microstructures for the two steels study seems to provide a clear impact of the cooling rate effect. For the SLM 4340, conventional microstructural components were observed at the slowest cooling rate, i.e. ferrite, pearlite, MA and Cr-carbides. When the cooling rate was increased after deformation, more complexes phases could be seen, especially for the cooling rate of 20°C/min. In this condition, martensite, bainite, granular bainite and MA could be observed throughout the sample. At the fastest cooling path, most of the SLM sample exhibited martensite and bainite, except for the presence of carbides-free bainitic ferrite. As expected, the water quenched samples were 100% martensitic.

For the wrought 4340, martensite and bainite were observed at cooling rates higher than 20°C/min. At this level of microstructural analysis, the wrought sample cooled at 1°C/min had the same behavior as the selective laser melted sample, according to phase distributions, i.e. ferrite, pearlite and MA. Again, as expected, for the water quenched samples, only martensite could be seen. Figure 41 shows a comparison for both alloys cooled at 20°C/min. The main difference between the samples is the presence of granular bainite in the SLM sample.

The microstructural results observed clearly indicates the strong effect of the fabrication technique, microstructural condition, and uniformity of the chemical composition of the steels used in this program. It is suspected that the carbon content and micro-segregation have a strong effect on the microstructural changes after continuous cooling paths, mainly after deformation. The starting microstructure also has an important effect on the final microstructure.

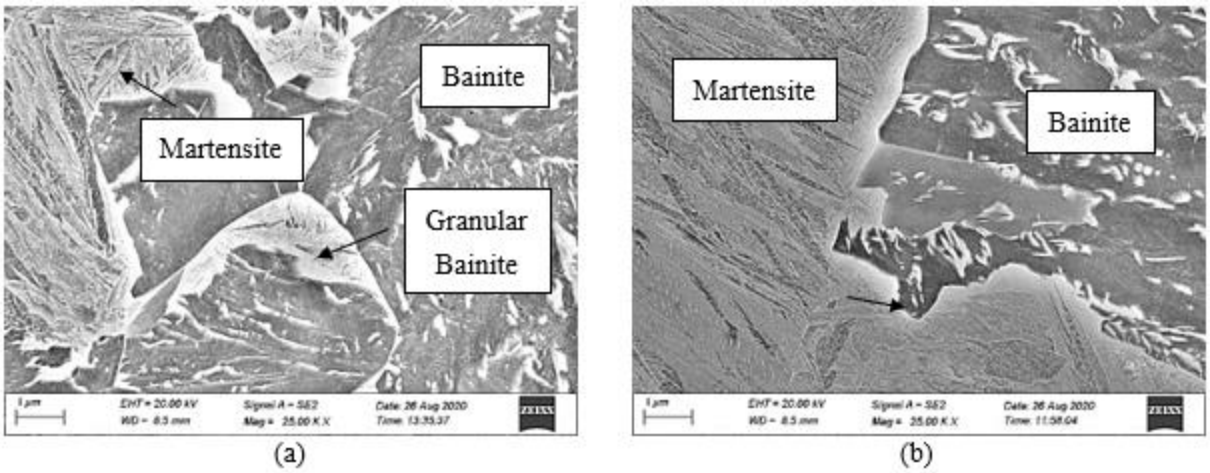

Figure 41 SEM (25kX mag) comparing the (a) SLM 4340 and (b) Wrought 4340 cooled at 20°C/min

7.4.3 Effect of Hardenability on Microstructure and Mechanical Property

Different starting microstructure, alloy element distribution, prior austenite grain size will affect the austenite-ferrite transformation behavior, even with similar chemical composition. These different conditions do affect the nucleation rate of ferrite and cementite during the cooling. Figure 43 and Figure 44 are IPF maps of SLM 4340 and wrought 4340. EBSD-IQ analysis are performed to measure the phase balance in this chapter. From this result, it can be observed that Wrought 4340 has higher hardenability, so austenite-martensite transformation happened at 20 ℃/min, causing higher hardness compared to SLM 4340. In our initial hypothesis, better mechanical properties of SLM 4340 compared to Wrought 4340 are expected due to finer microstructure and similar chemical composition. However, the HVN results indicated that the microstructures obtained from the wrought 4340 steel were harder than those from the SLM steel for all cooling rates studied. This result could be rationalized by hardenability. Wrought 4340 has higher hardenability due to coarser prior austenite grain size, so it has higher fraction of “hard” phase compared to SLM 4340 under each cooling condition. There is another explanation is that wrought

4340 has “stronger” boundary because of segregation of alloy element. This effect will be studied more deeply in future. Electron Probe Microanalysis (EPMA) will be used to study the difference in carbon content and micro-segregation between the samples.

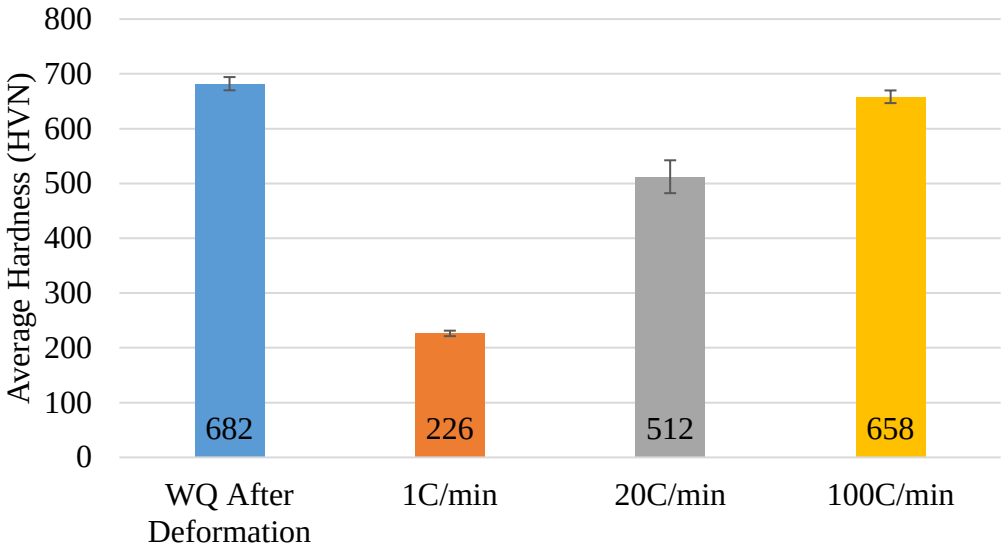

(a)

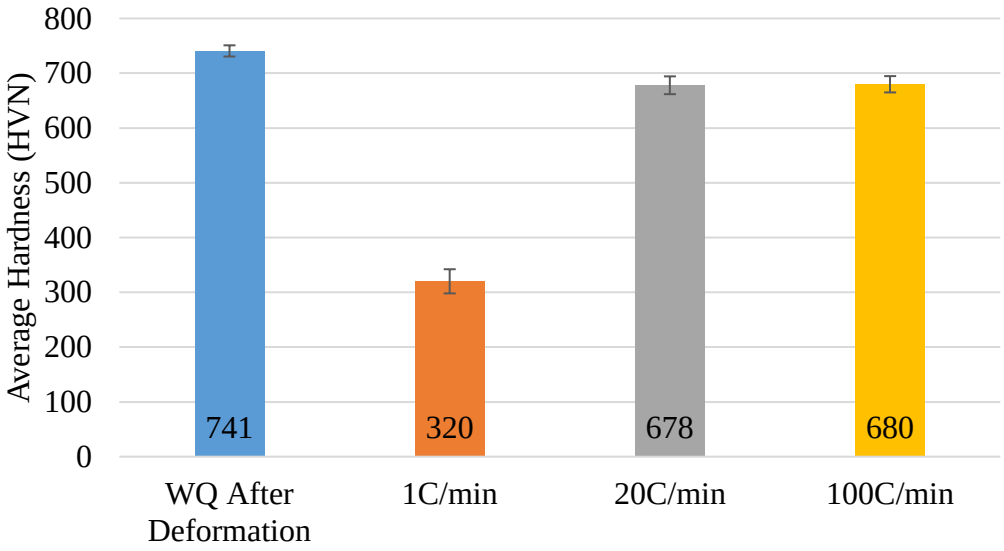

(b)

Figure 42 Hardness Measurements for (a) SLM 4340, and (b) wrought 4340 after hot compression testing

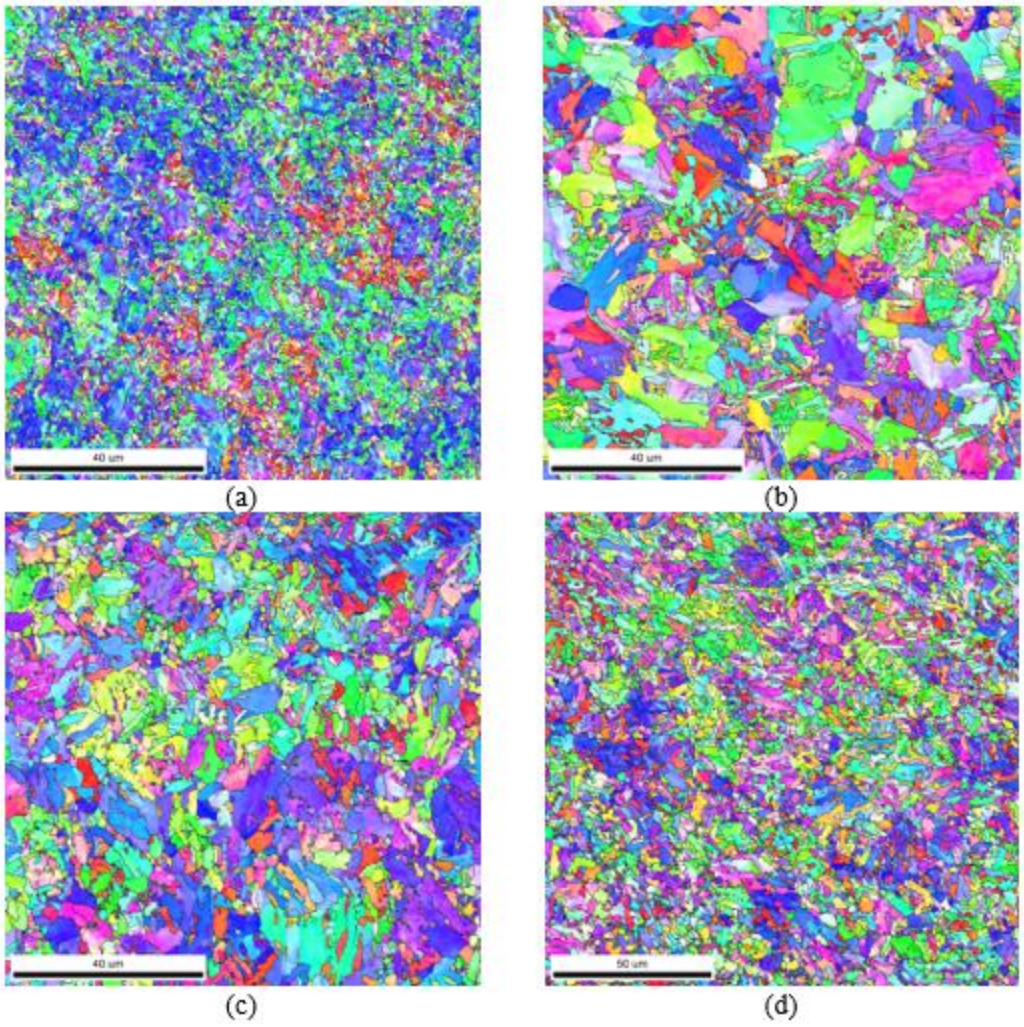

Figure 43 IPF Maps of hot deformed SLM 4340 cooled at (a) 1°C/min, (b) 20°C/min, (c) 100°C/min, (d)WQ

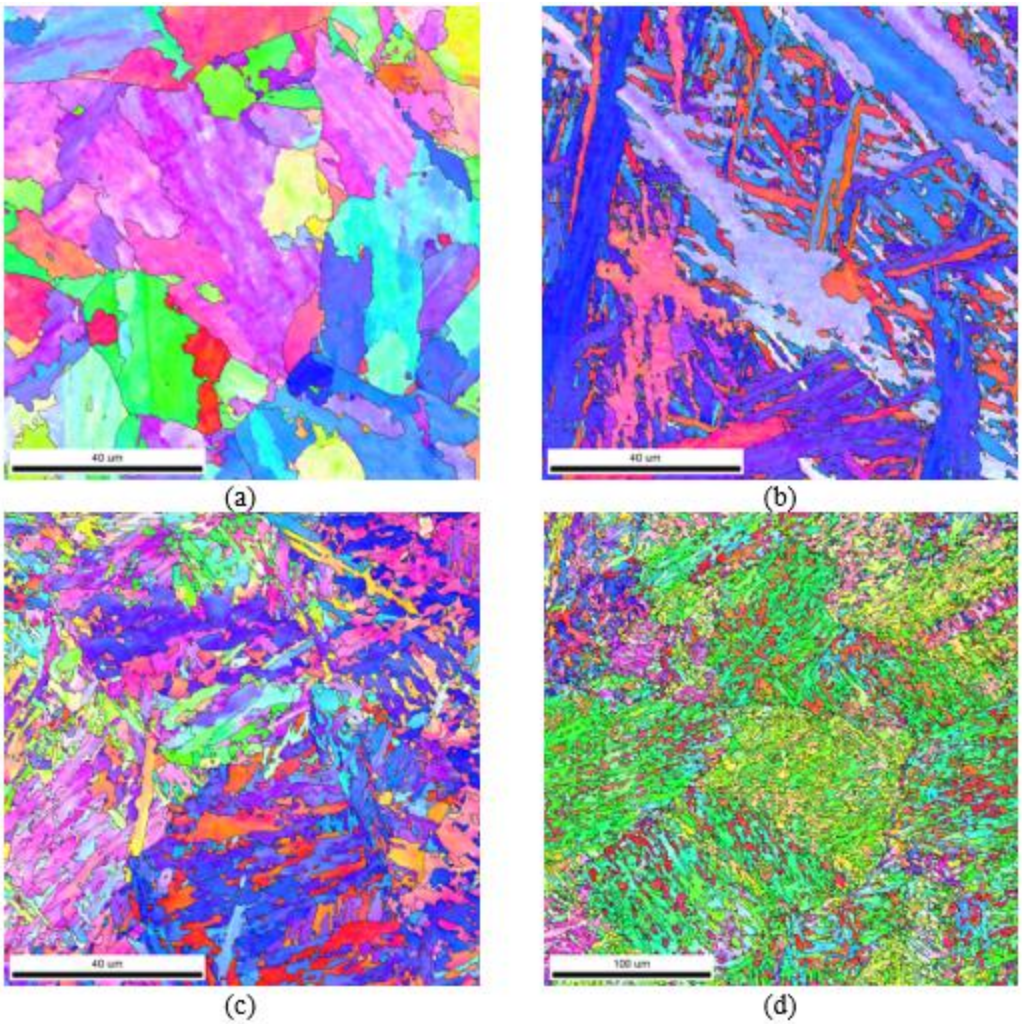

Figure 44 IPF Maps of hot deformed Wrought 4340 cooled at (a) 1°C/min, (b) 20°C/min, (c) 100°C/min, (d)WQ

8.0 Conclusions

This study provided a comprehensive understanding of SLM 4340 and developed continuous cooling transformation curves of both SLM 4340 and Wrought 4340. The effect of hot deformation on microstructure, transformation behavior, porosity density are investigated. Based on results and analysis, the following conclusion could be made:

Pinning effect of porosity is significant in SLM 4340. A small amount of porosity pinned austenite grain boundary during heat treatment, result in excellent austenite grain growth behavior.

Due to coarser prior austenite grain, wrought 4340 has higher hardenability than SLM 4340. Coarse austenite grain delay austenite-ferrite transformation under each cooling rate. The austenite-martensite transformation in wrought 4340 could be observed in dilatometric curve even cooling rate is decreased to 1℃/min.

Hot deformation is a necessary process for the application of SLM 4340. hot deformation eliminates most porosities in SLM 4340. However, the abnormal austenite grain growth is not observed after hot deformation. In summary, hot deformation could eliminate porosities and not cause grain coarsening in SLM 4340.

Wrought 4340 is harder than SLM 4340 at each cooling rate. This behavior could be rationalized by the effect of hardenability. High hardenability cause wrought 4340 have more fraction of hard phase at each cooling rate. The other explanation is the behavior of alloy elements, which need to be investigated by EPMA in future.

9.0 Future Work

Many tests, and experiments have been left for the future due to COVID-19 epidemic. Future work concerns deeper analysis of the behavior of alloy elements in these materials, new experiments (hot rolling and tempering), more mechanical properties tests (Tensile Test and Charpy Impact Test). This thesis has been mainly focused on the continuous cooling transformation behavior and hot deformation characteristics of Wrought 4340 and SLM 4340. Because these materials have similar chemical composition, the behavior of alloy element and effect of them on mechanical properties are not investigated in this thesis. The following ideas could be conducted in the future:

Electron Probe Micro-Analysis (EPMA) could be performed to investigate the behavior of alloy element. In previous study, EDS was performed on these materials. However, the alloy content is too low to be quantified by EDS. EPMA could acquire precise, quantitative analyses at very small sizes, so it may be helpful to analyze the behavior of alloy elements on grain boundaries and in ferrite matrix.

A tempering study will be conducted in future. Since the effect of hot deformation on SLM 4340 and Wrought 4340 are investigated in this thesis. And since quenched and tempering processing is the most common form of hardening and strengthening for 4340 steels, it is reasonable to compare the microstructure, mechanical properties of hot rolled plus WQ and tempering of SLM 4340 and Wrought 4340.

Bibliography

[1] Koh-ichi Sugitomo, Tomohiki, and, Yuta Mizuno, Torsional Fatigue Strength of newly Developed Case Hardening TRIP–Aided Steel, Metals, 375, 2017, p: 1-13.

[2] M.G.Hebsur, Recent Attempts of Improving the Mechanical Properties of AISI 4340 Steel by Control of Microstructure—A brief Review, American Society for Metals, 1982.

[3] Sharma SS, Prabhu PR, Gowri Shankar MC, Sudhakar AVB. Mechanical property assessment of austempered and conventionally hardened AISI 4340 Steel, Int J Mech Eng Technol (IJMET), 2014, 5(9):8-14.

[4] Niazi N, Aqueel Shah SN. Austempering, Heat Treatment of AISI 4340 Steel and comparative analysis of various physical properties at different parameters. Int J Multidiscip Sci Eng, 2014, 5(10).

[5] Torres MAS, Voorwald HJC. An evaluation of shot peening, residual stress and stress relaxation on the fatigue life of AISI 4340 steel. Int J Fatigue, 2002, 24(8):877-86.

[6] J,E, Pembertion, A.I. Guy, Properties and Selection: Irons Steels and High-Performance Alloys, ASM Handbook, vol. 1, ASM International, 1990. pp. 210-217.

[7] Majeed, A., Iqbal, A. & Lv, J. Enhancement of tool life in drilling of hardened AISI 4340 steel using 3D FEM modeling. Int J Adv Manuf Technol 95, 1875–1889 (2018). https://doi-org.pitt.idm.oclc.org/10.1007/s00170-017-1235-8

[8] Jelis, E., Hespos, M.R. & Ravindra, N.M. Process Evaluation of AISI 4340 Steel Manufactured by Laser Powder Bed Fusion. J. of Materi Eng and Perform 27, 63–71 (2018). https://doi-org.pitt.idm.oclc.org/10.1007/s11665-017-2989-8

[9] A. AHMADI, R. MIRZAEIFAR, N. S. MOGHADDAM, A. TURABI, H.E. KARACA, M. ELAHINIA. Effect of manufacturing parameters on mechanical properties of 316L stainless steel parts fabricated by selective laser melting: A computional framework. 2016

[10] Y. TOMITA, K. OKABAYASHI. Effect quench rate on microstructure and tensile properties of AISI 4320 and 4340 steels. 1987

[11] Tartaglia, J., Lazzari, K., Hui, G. et al. A Comparison of Mechanical Properties and Hydrogen Embrittlement Resistance of Austempered vs Quenched and Tempered 4340 Steel. Metall Mater Trans A 39, 559–576 (2008). https://doi.org/10.1007/s11661-007-9451-8

[12] BANDYOPADHYAY, A.; BOSE, S. Additive Manufacturing. Boca Raton: CRC Press, 2016. ISBN 9781482223590. Page: 1.

[13] L. Wood. Global Additive Manufacturing Market (2012–2017). Globe Newswire. Press Releases. CNBC LLC, Los Angeles, CA. 2014.

[14] SmarTech Analysis. 2020 Additive Manufacturing Market Outlook and Summary of Opportunities.

[15] G. Warwick. Print to Build. Aviation Week & Space Technology. 176(11):40–43, 2014.

[16] Eleonora Atzeni, Alessandro Salmi, Evaluation of additive manufacturing (AM) techniques for the production of metal–ceramic dental restorations, Journal of Manufacturing Processes, Volume 20, Part 1, 2015, Pages 40-45, ISSN 1526-6125.

[17] Slotwinski JA, Garboczi EJ, Hebenstreit KM. Porosity Measurements and Analysis for Metal Additive Manufacturing Process Control. J Res Natl Inst Stand Technol. 2014;119:494-528. Published 2014 Sep 16. doi:10.6028/jres.119.019

[18] D D Gu, W Meiners, K Wissenbach & R Poprawe, Laser Additive Manufacturing of Metallic Components: Materials, Processes and Mechanisms, International Materials Reviews, 57:3, 2012, 133-164.

[19] H. Attar, L. Löber, A. Funk, M. Calin, L.C. Zhang, K.G. Prashanth, S. Scudino, Y.S. Zhang, J. Eckert, Mechanical behavior of porous commercially pure Ti and Ti–TiB composite materials manufactured by selective laser melting, Materials Science and Engineering: A, Volume 625, 2015, Pages 350-356, ISSN 0921-5093.

[20] Joachim Gussone, Yves-Christian Hagedorn, Human Gherekhloo, Galina Kasperovich, Tarik Merzouk, Joachim Hausmann, Microstructure of γ-titanium aluminide processed by selective laser melting at elevated temperatures, Intermetallics, Volume 66, 2015, Pages 133-140, ISSN 0966-9795.

[21] Wei Li, Jie Liu, Yan Zhou, Shifeng Wen, Qingsong Wei, Chunze Yan, Yusheng Shi, Effect of substrate preheating on the texture, phase and nanohardness of a Ti–45Al–2Cr–5Nb alloy processed by selective laser melting, Scripta Materialia, Volume 118, 2016, Pages 13-18, ISSN 1359-6462.

[22] J.C. Wang, Y.J. Liu, P. Qin, S.X. Liang, T.B. Sercombe, L.C. Zhang, Selective laser melting of Ti–35Nb composite from elemental powder mixture: Microstructure, mechanical behavior and corrosion behavior, Materials Science and Engineering: A, Volume 760, 2019, Pages 214-224, ISSN 0921-5093.

[23] Yunjia Shi, Kun Yang, Shravan K. Kairy, Frank Palm, Xinhua Wu, Paul A. Rometsch, Effect of platform temperature on the porosity, microstructure and mechanical properties of an Al–Mg–Sc–Zr alloy fabricated by selective laser melting, Materials Science and Engineering: A, Volume 732, 2018, Pages 41-52, ISSN 0921-5093.

[24] Jelis, E., Hespos, M.R. & Ravindra, N.M. Process Evaluation of AISI 4340 Steel Manufactured by Laser Powder Bed Fusion. J. of Materi Eng and Perform 27, 63–71 (2018). https://doi-org.pitt.idm.oclc.org/10.1007/s11665-017-2989-8

[25] Fe-C diagram, 10.03 2020 by Andreas Velling. https://fractory.com/iron-carbon-phase-diagram/

[26] Einkhah F*, Rassizadehghani J and Najafidejdehmonfared H. The Effects of Microalloying Elements and Temperaging Treatments Parameters on Nb-V Containing Cast Microalloyed Steels

[27] F. Osmond, Méthode générale pour l'analyse micrographique des aciers au carbone, Bulletin de la societe d'Encouragement pour l'Industrie National, Vol 10, 1895, p 480

[28] Steels—Processing, Structure, and Performance, Second Edition. Page 64.

[29] E.A. Wilson, The c to a Transformation in Low Carbon Irons, ISIJ Int. 1994, Vol 34, p615-630

[30] H.K.D.H. Bhadeshia, Bainite in Steels, Book No. 504, The Institute of Materials, London, 1992

[31] Schematic representation of the transition from upper to lower bainite, After Takahashi and Bhadeshia (1990)

[32] M. Militzer, M.G. Mecozzi, J. Sietsma, S. van der Zwaag, Three-dimensional phase field modelling of the austenite-to-ferrite transformation, Acta Materialia, Volume 54, Issue 15, 2006, Pages 3961-3972

[33] Minoru UMEMOTO, Hideyuki OHTSUKA, Imao TAMURA, Transformation to Pearlite from Work-hardened Austenite, Transactions of the Iron and Steel Institute of Japan, 1983, Volume 23, Issue 9, Pages 775-784

[34] C. Ouchi, T. Sampei, I. Kozasu, The effect of hot rolling condition and chemical composition on the onset temperature of γ-α transformation after hot rolling, Trans. Iron Steel Inst. Japan 22 (1982) 214–222.

[35] Zakerinia, H., Kermanpur, A., and Najafizadeh, A., "The Effect of Bainite in Producing Nano/Ultrafine Grained Steel by the Martensite Treatment," Mater. Sci. Eng., Vol. 528, Nos. 10–11, 2011, pp. 3562–3567.

[36] Saraf, L. (2011). Kernel Average Misorientation Confidence Index Correlation from FIB Sliced Ni-Fe-Cr alloy Surface. Microscopy and Microanalysis, 17(S2), 424-425. doi:10.1017/S1431927611002996

[37] Jinghui WU, Peter J. WRAY, Calixto I. GARCIA, Mingjian HUA, Anthony J. DEARDO, Image Quality Analysis: A New Method of Characterizing Microstructures, ISIJ International, 2005, Volume 45, Issue 2, Pages 254-262.

[38] Ryan Barrows. Revealing Prior Austenite Grain Boundaries of 4340 Steel. California Polytechnic State University.

[39] S.V. Sajadifar, M. Ketabchi, B. Bemanizadeh. Dynamic recrystallization behavior and hot deformation charactetistics in 4340 steel.

[40] Nyyssönen, T.; Isakov, M.; Peura, P.; Kuokkala, V.-T. Iterative Determination of the Orientation Relationship Between Austenite and Martensite from a Large Amount of Grain Pair Misorientations. Metall. Mater. Trans. A 2016, 47, 2587–2590.

[41] Nyyssönen, T.; Peura, P.; Kuokkala, V.-T. Crystallography, Morphology, and Martensite Transformation of Prior Austenite in Intercritically Annealed High-Aluminum Steel. Metall. Mater. Trans. A 2018, 49, 6426–6441.

[42] K.D. Zilnyk, G.S. Leite, H.R.Z. Sandim, P.R. Rios, Grain growth inhibition by connected porosity in sintered niobium, Acta Materialia, Volume 61, Issue 15, 2013, Pages 5821-5828, ISSN 1359-6454.

[43] Y. Liu, B.R. Patterson, Grain growth inhibition by porosity, Acta Metallurgica et Materialia, Volume 41, Issue 9, 1993, Pages 2651-2656, ISSN 0956-7151.

[44] L. E. Collins, R. F. Knight, G. E. Ruddle and J. D. Boyd: Proc. of Int. Symp. on Accelerated Cooling of Steel, ed, by P. D. Southwick, Pittsburgh, 1985, 261.

[45] Y. E. Smith, C. A. Siebert, Metall. Trans, ASM, 2A, 1971, 1711.

[46] H. Scott, G. Sidhu, F. Fazeli, A. K. Pilkey & J. D. Boyd (2017) Microstructural evolution of a hot-rolled microalloyed complex phase steel, Canadian Metallurgical Quarterly, 56:1, 67-75, DOI: 10.1080/00084433.2016.1252555.

[47] Virendra S. Warke, Richard D. Sisson, Makhlouf M. Makhlouf, The effect of porosity on the Austenite to Ferrite transformation in powder metallurgy steels, Materials Science and Engineering: A, Volume 528, Issues 10–11, 2011, Pages 3533-3538, ISSN 0921-5093.

[48] S. Sekino, N. Mori and S. Tamukai: Tetsu-to-Hagane, 59 (1973), 1418.

[49] T. M. Hoogendooren and M. J. Spanraft: Proceedings of Microalloying 75, Union Carbide Corp., New York, (1977), 75.

[50] T. Tanaka and N. Tabata : Tetsu-to-Hagane, 64 (1978), 1353.

[51] R. Priestner and M. S. Biring: Metal Sci. J., 7 (1973), 60.

[52]M. Fukuda and K. Kunishige : T etsu-to-Hagane, 58 (1972), 1833.